

4.0 ASSESSMENT OF WAVE CLIMATE IMPACT BY OFFSHORE BORROW SITES

Excavation of an offshore borrow site can affect wave heights and the direction of wave propagation. The existence of an excavated hole or trench on the OCS can cause waves to refract toward the shallow edges of a borrow site. This alteration to a wave field by a borrow site may change local sediment transport rates, resulting in some areas experiencing a reduction in longshore transport and other areas showing an increase. To determine potential physical impacts associated with dredging borrow sites offshore the central east coast of Florida, wave transformation modeling and sediment transport potential calculations were performed for existing and post-dredging bathymetric conditions. Comparison of computations for existing and post-dredging conditions illustrated the relative impact of borrow site excavation on wave-induced coastal processes.

The most effective means of quantifying physical environmental effects of sand dredging from shoals on the continental shelf is through use of wave transformation numerical modeling tools that recognize the random nature of incident waves as they propagate onshore. Spectral wave models, such as STWAVE (STeady-state spectral WAVE model), REF/DIF-S (REFraction/ DIFfraction model for Spectral wave conditions), SWAN (Simulation of Waves Nearshore), and others, typically provide more realistic results than monochromatic wave models relative to field measurements. As such, spectral wave transformation modeling was applied in this study to evaluate potential impacts to coastal and nearshore sites from long-term dredging and significant removal of sand from offshore sand borrow sites. Although interpretation of wave modeling results is relatively straightforward, evaluating the significance of predicted changes for accepting or rejecting a borrow site is more complicated.

As part of any offshore sand mining effort, the MMS requires an evaluation of potential environmental impacts associated with alterations to nearshore wave patterns. To determine potential physical impacts associated with borrow site excavation, the influence of borrow site geometry on local wave refraction patterns was evaluated. Because large natural spatial and temporal variability exists within the wave climate at a particular site, determination of physical impacts associated with sand mining must consider the influence of process variability. A method based on historical wave climate variability, as well as local wave climate changes directly attributable to borrow site excavation, has been applied to determine appropriate criteria for assessing impact significance.

To directly assess impacts to coastal processes associated with sand mining, an approach was utilized that considers spatial (longshore) and temporal aspects of the local wave climate, as described by Kelley et al. (2004). This method was applied by performing wave model runs using mean conditions developed from the entire 20-year WIS record, and then 20 year-long blocks of the WIS record to determine annual variability of the wave climate along this shoreline. In this manner, temporal variations in wave climate are considered relative to average annual conditions. From these wave model runs, sediment

transport potential curves are derived for average annual conditions (based on the full 20-year WIS record) and each 1-year period (based on the 20 1-year wave records parsed from the full record). Applying this information, the average and standard deviation in calculated longshore sediment transport potential are determined every 200 m along the shoreline.

Assuming the temporal component of sediment transport potential is normally distributed, the suggested criterion for accepting or rejecting a potential borrow site is based on a range of one standard deviation about the mean. As proposed, the criterion would require that if any portion of the sediment transport potential curve associated with a sand mining project exceeds one-half the standard deviation of natural temporal variability in sediment transport potential, the site would be rejected. Conversely, a borrow site design would be accepted as long as the transport potential change determined for post-dredging conditions at a site occurs within the range of one-half the standard deviation.

The natural variability envelope provides a basis for judging the impacts of a borrow site relative to sediment transport processes along a coastline. Because there is a greater than 50% chance that the transport computed for a particular year will occur outside the $\pm 0.5\sigma$ envelope about the mean, impacts determined for a particular borrow site that occur within this range will be indistinguishable from observed natural variations.

An example of this method taken from previous work (Byrnes et al., 2003) is shown in Figure 4-1, where alterations in wave climate caused by dredging a series of borrow sites offshore northeastern North Carolina were determined to be insignificant relative to natural variability. For the modeled shoreline, the area where computed change in transport potential comes closest to exceeding the significance envelope was at a shoreline point near N 3,967,000 UTM. At this location, transport potential change was determined to be approximately 30,000 m³/yr, which was less than the approximate 40,000 m³/yr allowable limit of change set by the significance criterion. Due to the relatively high natural variability in wave climate in this area, simulated shoreline change induced by offshore borrow site dredging could not be identified relative to natural changes. For this reason, sites with large natural variation in wave climate and associated sediment transport potential may have larger simulated impacts associated with an offshore sand mining project.

As a management tool for the MMS, this methodology provides several advantages over methods previously employed to assess the significance of borrow site impacts. The primary advantages include:

1. Observed long-term shoreline change is compared with computed longshore change in sediment transport potential. Close comparison between these two curves indicates that longshore sediment transport potential calculations are appropriate for assessing long-term natural change. Therefore, this methodology has a model-independent component (observed shoreline change) used to ground truth model results.
2. The method is directly related to sediment transport potential and associated shoreline change. Therefore, impacts associated with borrow site excavation can be directly related to their potential influence on observed coastal processes (annualized variability in shoreline position).

3. Site-specific temporal variability in wave climate and sediment transport potential is calculated as part of the methodology. For sites that show little natural variability in inter-annual wave climate, coastal processes impacts associated with borrow site dredging similarly would be limited, and *vice versa*. In this manner, the inter-annual temporal component of the natural wave climate is a major component in determining impact significance.
4. Similar to methodologies incorporated in previous MMS studies, the longshore spatial distribution of borrow site impacts was considered. However, an acceptable limit of longshore sediment transport variability was computed from the temporal component of the analysis. Therefore, the final results of this analysis provided a spatially-varying envelope of natural variability in addition to the modeled impacts directly associated with borrow site excavation. The methodology accounts for spatial and temporal variability in wave climate, as well as providing a defensible means of assessing significance of impacts relative to site-specific conditions.

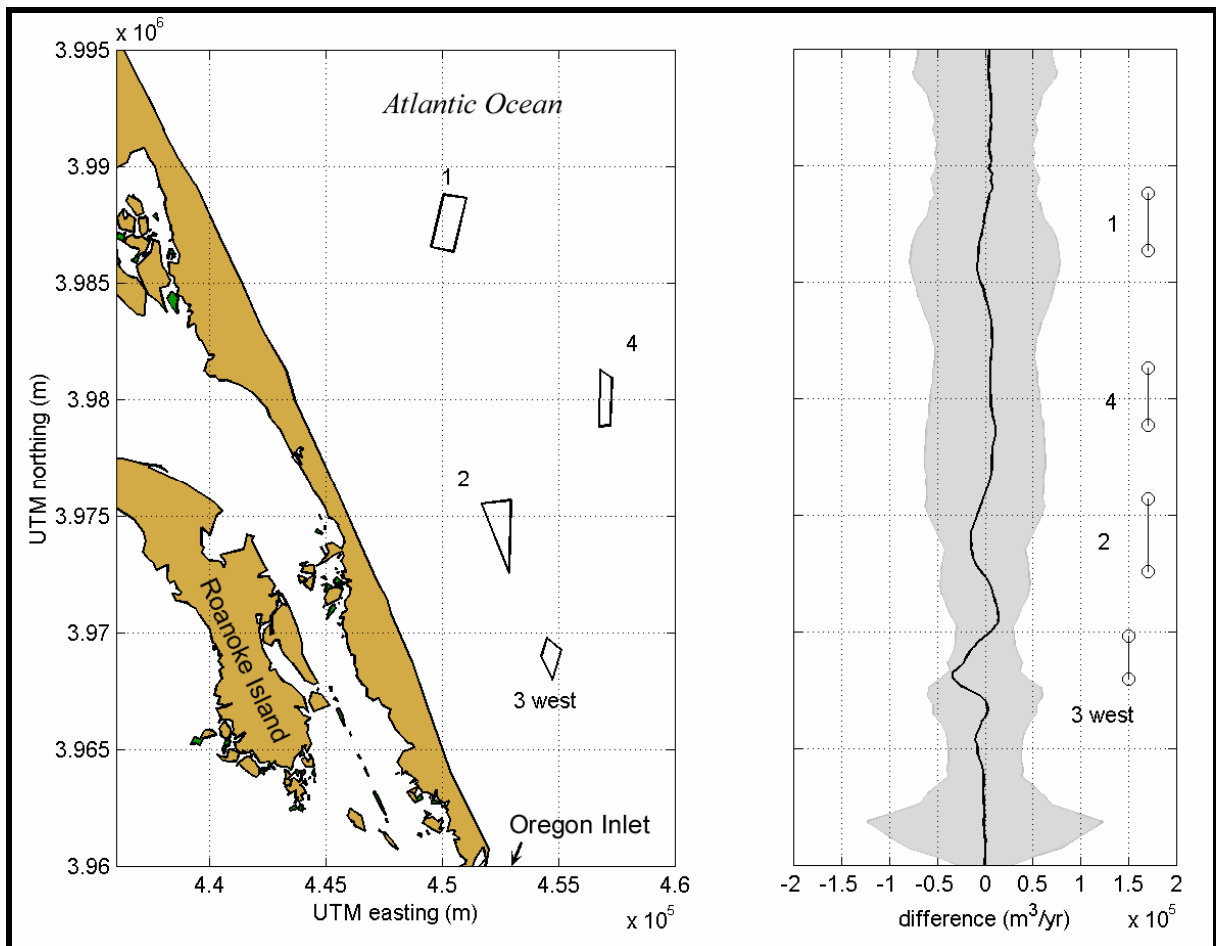


Figure 4-1. Natural variability in sediment transport potential for determining significance of borrow site dredging impacts (Byrnes et al., 2003). The difference plot illustrates modeled change in net transport potential (solid black line) resulting from dredging four borrow sites offshore North Carolina. The plot also shows the dredging significance criterion envelope ($\pm\sigma$) determined for this shoreline (gray-shaded envelope).

4.1 ANALYSIS APPROACH

Sediment transport rates along a coastline are dependent on local wave climate. For this study, nearshore wave heights and directions along the shoreline landward of proposed borrow sites were estimated using the USACE spectral wave model STWAVE, which was used to simulate the propagation of offshore waves to the shoreline. Offshore wave data available from WIS were used to derive input wave conditions for STWAVE.

4.1.1 Wave Modeling

Developed by the USACE Waterways Experiment Station (WES), STWAVE v2.0 is a steady state, spectral wave transformation model (Smith et al., 1999). Two-dimensional (frequency and direction versus energy) spectra were used as input to the model. STWAVE is able to simulate wave refraction and shoaling induced by changes in bathymetry and by wave interactions with currents. The model includes a wave breaking model based on water depth and wave steepness. Model output includes significant wave height (H_s), peak wave period (T_p), and mean wave direction ($\bar{\theta}$).

STWAVE is an efficient program that requires minimal computing resources to run well. The model is implemented using a finite-difference scheme on a regular Cartesian grid (grid increments in the x and y directions are equal). During a model run, the solution is computed starting from the offshore open boundary and is propagated onshore in a single pass of the model domain. As such, STWAVE can propagate waves only in directions within the $\pm 87.5^\circ$ half plane. A benefit of using this single pass approach is that it uses minimal computer memory because the only memory-resident spectral data are for two grid columns. Accordingly, changing wave spectra across each grid column are computed using information solely from the previous grid column.

STWAVE is based on a form of the wave action balance equation. The wave action density spectrum, which includes the effects of currents, is conserved along wave rays. In the absence of currents, wave rays correspond to wave orthogonals, and the action density spectrum is equivalent to the wave energy density spectrum. A diagram showing the relationship of wave orthogonal, wave ray, and current directions is shown in Figure 4-2. The governing equation of wave transformation, using the action balance spectrum, in tensor notation is written as (Smith et al., 1999)

$$(C_{ga})_i \frac{\partial}{\partial x_i} \frac{C_a C_{ga} \cos(\mu - \alpha) E}{\omega_r} = \sum \frac{S}{\omega_r} \quad (4.1)$$

where

- $E = E(f, \theta)$ wave energy density spectrum,
- S = energy source and sink terms (e.g., white capping, breaking, wind input),
- α = wave orthogonal direction,
- μ = wave ray direction (direction of energy propagation),
- ω_r = relative angular frequency ($2\pi f_r$),
- C_a, C_{ga} = absolute wave celerity and group celerity, respectively.

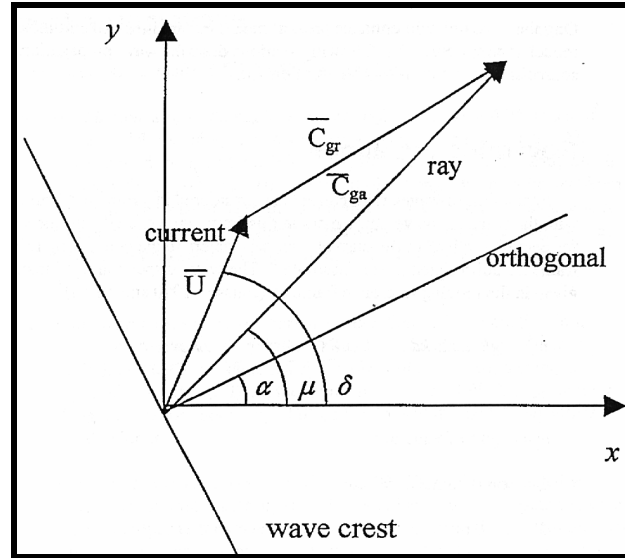


Figure 4-2. Wave and current vectors used in STWAVE. Subscript *a* denotes values in the *absolute* frame of reference, and subscript *r* denotes values in the *relative* frame of reference (with currents).

The breaking model in STWAVE is based on a form of the Miche criterion as discussed by Battjes and Janssen (1978). It sets a maximum limit on the zero-moment wave height (H_{mo}), the wave height based on the distribution of energy in the wave spectrum. The formulation of this model is

$$H_{mo(max)} = 0.1L \tanh(kd) \quad (4.2)$$

where L is the wavelength, k is the wave number ($k = 2\pi/L$), and d is the depth at the point where the breaking limit is being evaluated. This equation is used together with a simpler breaking model, which was used alone in earlier versions of STWAVE, where the maximum H_{mo} wave height is always expressed as a constant ratio of water depth

$$H_{mo(max)} = 0.64 d \quad (4.3)$$

An advantage of using Equation 4.2 over Equation 4.3 is that it accounts for increased wave breaking resulting from wave steepening caused by wave-current interactions. Once model wave heights exceed $H_{mo(max)}$, STWAVE uses a simple method to reduce the energy spectrum to set the value of $H_{mo} = H_{mo(max)}$. Energy at each frequency and direction is reduced by the same percentage. As a result, non-linear transfers of energy to high frequencies during breaking are not included in STWAVE.

4.1.1.1 Input Spectra Development

Offshore wave conditions used as input for wave modeling can be derived from two main sources: measured spectral wave data from offshore data buoys or hindcast simulation time series data (Hubertz et al., 1993). In general, buoy data are the preferred source of wave information for modeling because they represent actual offshore measurements rather than hindcast information derived from large-scale models. However, very few sites along the U.S. east coast have wave measurement records of sufficient length to justify their use as a source of long-term information. Offshore central east Florida, sources of measured

directional wave data include the Florida Coastal Data Network (CDN) (Wang et al., 1990) and various short-term deployments of individual gages (e.g., the 1991 University of Florida deployment of a PUV gage offshore Jupiter Island [Harris, 1991]). Past comparisons of WIS hindcast data and waves measured offshore eastern Florida illustrated general agreement (Ramsey et al., 1995), suggesting that WIS hindcast data sets are a valid source of wave data for this study.

Wave input conditions for simulations offshore central east Florida were developed using hindcast data from WIS Stations AU2019 (19) for Area A, AU2016 (16) for Area B, AU2014 (14) for Area C, and AU2013 (13) for Area D. Locations of these WIS stations are shown with the limits of computational grids in Figure 4-3. WIS records cover a 20-year period from January 1976 to December 1995. Station 19 is located approximately 29 km east-northeast of Cape Canaveral in 35 m water depth. Station 16 is located in 45 m water depth approximately 45 km east of Sebastian Inlet. Station 14 is located in 55 m water depth approximately 18 km east of St. Lucie Inlet, and Station 13 is located approximately 10 km east of Jupiter Inlet in 45 m water depth.

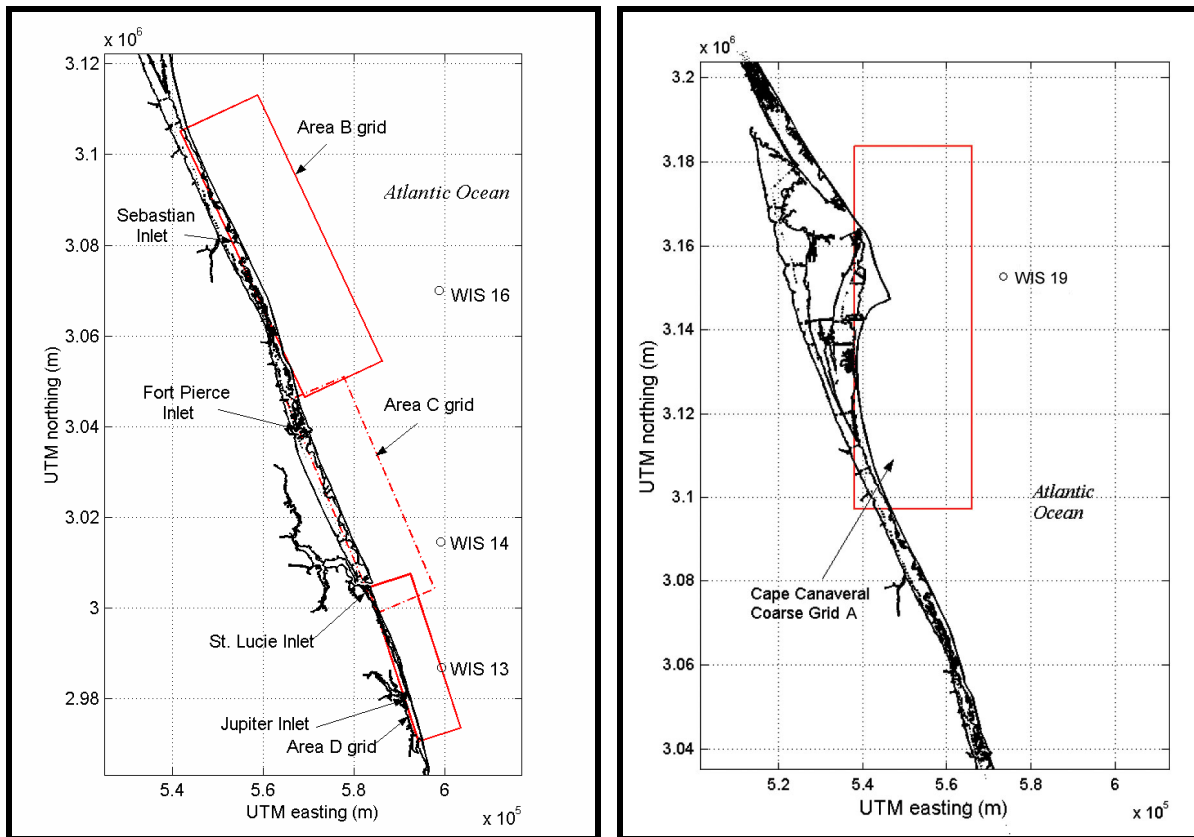


Figure 4-3. Shoreline of central east Florida with coarse grid limits and WIS stations used to evaluate potential dredging impacts from offshore sand mining.

Two wave roses showing percent occurrence of different wave conditions for each of the four WIS stations are shown in Figures 4-4 through 4-7. The first rose for Station 19 illustrates variations in wave height distribution by direction (Figure 4-4). Most waves (90%) in the record occur within the 30° and 120° compass sector, and the greatest percentage of waves (43%) is from the east-northeast. Mean height for all waves in the record is 1.3 m, and the standard deviation is 0.7 m. Mean height for waves along the dominant wave

direction is 1.4 m, with a standard deviation of 0.7 m. The second rose in Figure 4-4 illustrates the distribution of peak wave period in the record. Mean peak period for the entire record is 9.3 sec, and 38% of simulated waves have peak periods greater than 9 sec.

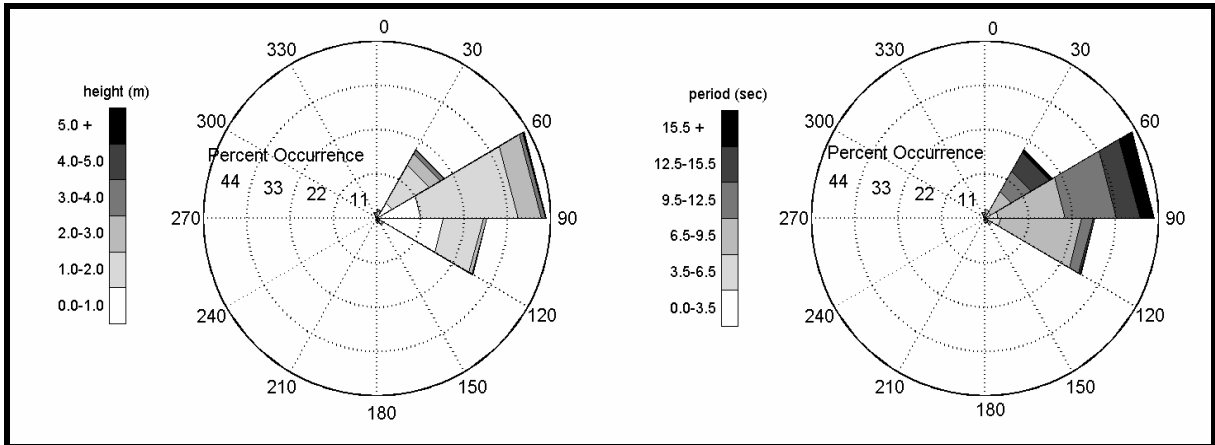


Figure 4-4. Wave height and period for hindcast data from WIS station AU2019, January 1976 and December 1995. Direction indicates from where waves were traveling, relative to true north. Radial length of gray tone segments indicates percent occurrence for each range of wave height and period.

Wave plots for Station 16 are illustrated in Figure 4-5. Most waves (89%) in the WIS record occur within the compass sector between 30° and 120°. Dominant wave direction is between 60° and 90°, from which 45% of waves in the record propagate. Mean height for all waves in the record is 1.3 m, and the standard deviation is 0.7 m. Mean height for waves from the dominant wave direction is 1.4 m, and the standard deviation is 0.7 m. The second rose in Figure 4-5 shows the distribution of peak wave period in the record. A significant number of wave events (38%) have peak periods greater than 9 sec, and the mean peak period for the entire record is 9.3 sec.

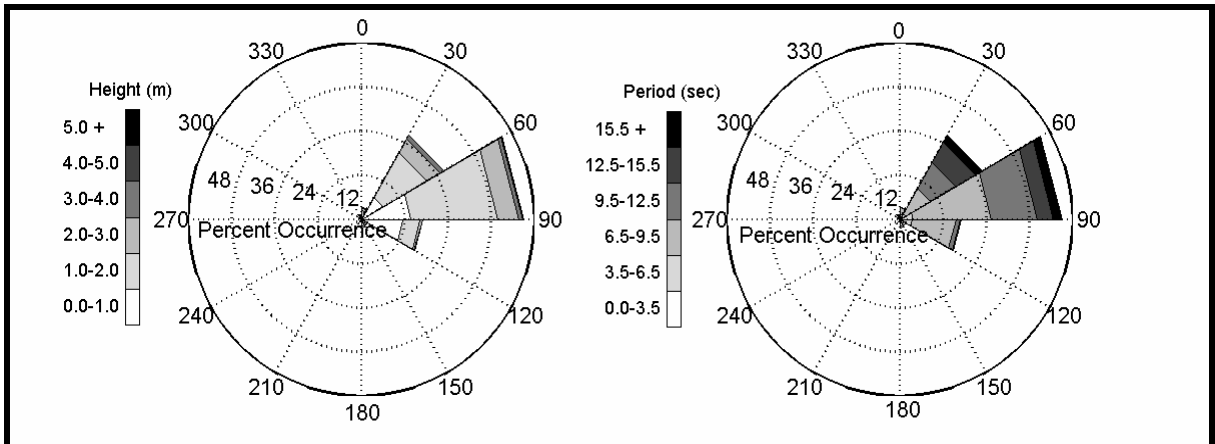


Figure 4-5. Wave height and period for hindcast data from WIS Station AU2016, January 1976 and December 1995. Direction indicates from where waves were traveling relative to true north. Radial length of gray tone segments indicates percent occurrence of each range of wave height and period.

Wave plots for Station 14 are shown in Figure 4-6. Most waves (76%) occur within the 30° and 90° compass sector. Dominant wave direction is between 30° and 60°, from which 39% of waves in the record propagate. Mean height for all waves is 1.2 m, with a standard deviation of 0.7 m. Mean height for waves from the dominant direction is 1.3 m, and the standard deviation is 0.7 m. A significant number of wave events (40%) have peak periods greater than 9 sec, and the mean peak period for the entire record is 9.1 sec.

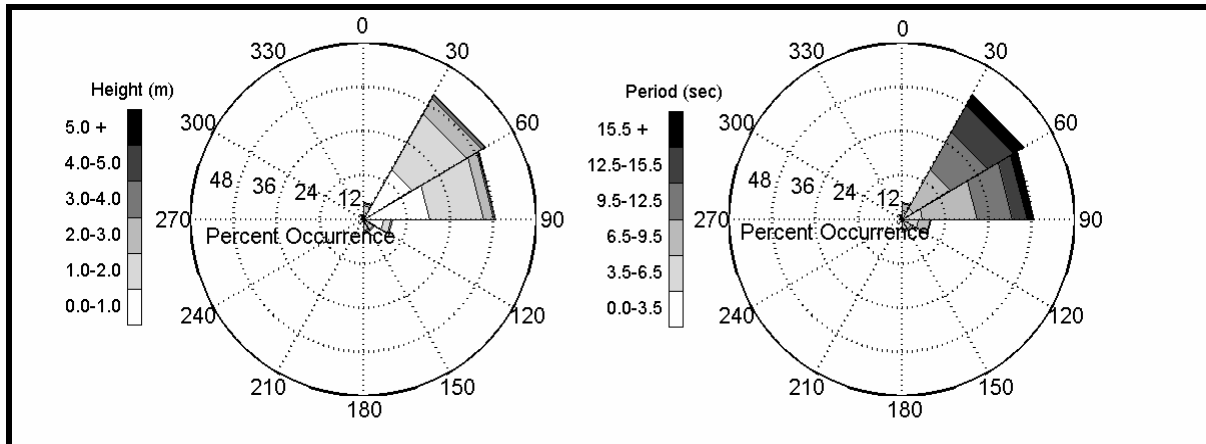


Figure 4-6. Wave height and period for hindcast data from WIS Station AU2014, January 1976 and December 1995. Direction indicates from where waves were traveling relative to true north. Radial length of gray tone segments indicates percent occurrence of each range of wave height and period.

Plots for Station 13, offshore Jupiter Inlet, illustrate that most waves (73%) propagate onshore from between 30° and 90° (Figure 4-7). Similar to Station 14, dominant wave direction is between 30° and 60°, from which 44% of waves in the record propagate. Mean height for all waves in the record is 1.1 m, and the standard deviation is 0.7 m. Mean wave height from the dominant wave direction is 1.1 m, and the standard deviation is 0.7 m. For wave period, a significant number of wave events (38%) have peak periods greater than 9 sec, and the mean peak period for the entire record is 8.8 sec.

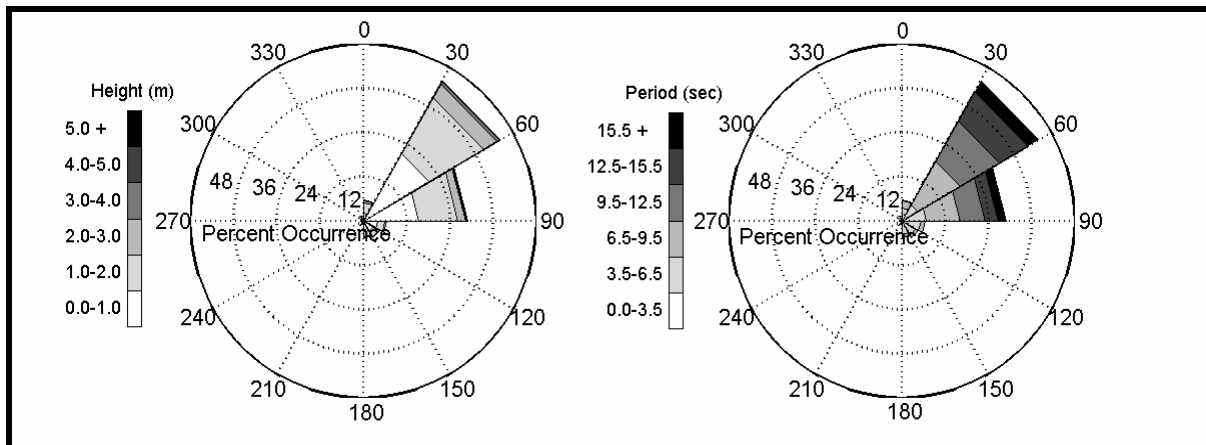


Figure 4-7. Wave height and period for hindcast data from WIS Station AU2013, January 1976 and December 1995. Direction indicates from where waves were traveling relative to true north. Radial length of gray tone segments indicates percent occurrence of each range of wave height and period.

WIS station plots illustrate that the dominant direction of wave propagation shifts northward from Station 19 to Station 13. This results from the combined influence of the Florida Current and the sheltering effect of Bahama Bank, 100 km east of Jupiter Inlet. There also is a general trend of slightly smaller wave heights and shorter wave periods for the southernmost WIS Station (13) compared with Station 19.

STWAVE input spectra were developed using a numerical routine that recreates a two dimensional spectrum for each individual wave condition in the WIS record. The program computes the frequency and directional spread of a wave energy spectrum based on significant wave parameters (i.e., wave height, peak period, and peak direction) and wind speed (Goda, 1985). The frequency spectrum $S(f)$ is computed using the relationship

$$S(f) = 0.257 H_{1/3}^2 T_{1/3} (T_{1/3} f)^{-5} \exp[-1.03(T_{1/3} f)^{-4}] \quad (4.4)$$

known as the Bretschneider-Mitsuyasu spectrum, where $H_{1/3}$ is the significant wave height, f is the discrete frequency where $S(f)$ is evaluated, and $T_{1/3}$ is the significant period, estimated from the peak wave frequency (f_p) by

$$T_{1/3} = 1/(1.05f_p) \quad (4.5)$$

To compute the two-dimensional energy spectrum, a directional spreading function $G(f, \theta)$ must be applied to the frequency spectrum such that

$$S(f, \theta) = S(f)G(f, \theta) \quad (4.6)$$

In this method, the directional spreading function is computed using the relationship

$$G(f, \theta) = G_o \cos^{2s} \left(\frac{\theta}{2} \right) \quad (4.7)$$

where s is a spreading parameter related to wind speed and frequency, θ is the azimuth angle relative to the principle direction of wave travel, and G_o is a constant dependent on θ and s . The spreading parameter s is evaluated using the expression

$$s = \begin{cases} s_{\max} \cdot (f/f_p)^5 & : f \leq f_p \\ s_{\max} \cdot (f/f_p)^{-2.5} & : f \geq f_p \end{cases} \quad (4.8)$$

where $s_{\max} = 11.5(2\pi f_p U/g)^{-2.5}$. Wind speed U is therefore used to control the directional spread of the spectrum by increasing the directional spread with increasing wind speed. Finally, the constant G_o is computed by evaluating the integral

$$G_o = \left[\int_{\theta_{\min}}^{\theta_{\max}} \cos^{2s} \left(\frac{\theta}{2} \right) d\theta \right]^{-1} \quad (4.9)$$

The result is a wave energy spectrum that is based on parameters from the WIS record, and that distributes spectral energy based on wave peak frequency and wind speed. An example of a two-dimensional spectrum generated by this method is presented in Figure 4-8.

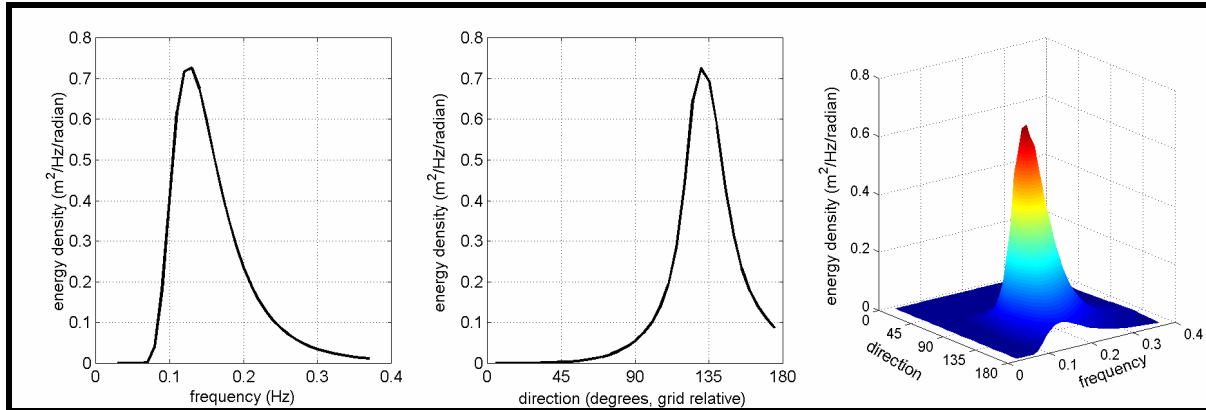


Figure 4-8. STWAVE input spectrum developed using WIS 20-year hindcast data with Goda (1985) method of computing frequency and direction spectrum. Plots show a) frequency distribution of energy at peak direction, b) directional distribution of energy at peak frequency, and c) surface plot of two-dimensional energy spectrum ($H_{mo} = 0.9$ m, $\theta_{mean} = 130^\circ$ grid relative).

After recreating a two-dimensional spectrum from the parameters given in the WIS record, each individual spectrum is sorted, or “binned,” by peak direction and peak period. Wave spectra computed from wave parameters that occur within the limits of individual direction and period bins are added, and a mean spectrum for all waves in each bin is computed based on total number of wave events in the bin. In total, seven direction bins and two period bins were used to characterize wave data. From 12 total bins, conditions used in STWAVE model runs were selected based on percent occurrence and percent energy for conditions in each bin.

Selected conditions have a percent occurrence greater than 1%, and also contain more than 1% of the energy of the entire wave record. Conditions selected for model runs are shown in Tables 4-1 to 4-4, with the significant parameters of each input spectrum.

4.1.1.2 Grid Development

Input spectra and two coarse grids were developed for each sand resource area for simulating wave propagation over existing and post-dredging bathymetry. A fine grid, nested within coarse grids, was developed for each area to obtain greater resolution of wave characteristics in the nearshore, landward of borrow sites. Most recent surveys (see Section 3.0) were the primary source of bathymetric data for creating grids. However, these data were supplemented by more recent local bathymetric data where available. Contour plots of existing conditions grids for each modeled area are shown in Figures 4-9 (Area A), 4-10 (Area B), 4-11 (Area C), and 4-12 (Area D).

Table 4-1. Input wave spectra parameters used for existing and post-dredging STWAVE runs for modeled Area A.

	STWAVE Model Input Condition	Percent Occurrence	H_{m0} Wave Height (m)	Peak Wave Period, T_p (sec)	Peak Wave Direction, θ_p ($^\circ$ true north)	Peak Wave Direction, θ_p (grid relative)	Direction Bin (grid relative)
Period Band 1	1A	8.2	1.7	7.7	55	55	30-60
	2A	20.8	1.4	7.7	80	80	60-90
	3A	24.6	1.0	7.7	100	100	90-120
	4A	2.3	1.5	6.3	130	130	120-150
Period Band 2	5A	6.5	1.7	12.5	60	60	30-60
	6A	28.5	1.6	14.3	65	65	60-90
	7A	3.4	1.5	11.1	100	100	90-120

Table 4-2. Input wave spectra parameters used for existing and post-dredging STWAVE runs for modeled Area B.

	STWAVE Model Input Condition	Percent Occurrence	H_{m0} Wave Height (m)	Peak Wave Period, T_p (sec)	Peak Wave Direction, θ_p ($^\circ$ true north)	Peak Wave Direction, θ_p (grid relative)	Direction Bin (grid relative)
Period Band 1	1B	2.3	1.9	6.9	25	50	33.75-56.25
	2B	6.5	1.8	7.6	45	70	56.25-78.75
	3B	7.0	1.6	7.7	60	85	78.75-90.00
	4B	7.2	1.5	7.7	70	95	90.00-101.25
	5B	24.7	1.1	7.7	90	115	101.25-123.75
	6B	5.7	1.1	6.9	105	130	123.75-146.25
Period Band 2	7B	6.7	1.7	11.4	50	75	56.25-78.75
	8B	15.7	1.7	13.9	60	85	78.75-90.00
	9B	8.4	1.7	12.4	70	95	90.00-101.25
	10B	6.6	1.7	10.8	90	115	101.25-123.75

Dimensional characteristics of each grid are presented in Table 4-5. Geographical limits for each grid were chosen based on wave conditions selected for model simulations. Wave conditions with relatively small angles to the shoreline require a wide grid so the area of potential impact does not occur within the shadow of the lateral grid boundaries. Depths at the offshore boundary of the coarse grid for Area A ranged from 19 to 30 m (relative to the National Geodetic Vertical Datum [NGVD]), and the grid extends about 87 km alongshore. The coarse grid for Area B covers a region that extends approximately 17 km offshore and 65 km alongshore. Depths at the offshore boundary vary between 11 and 24 m (NGVD), with a mean depth of approximately 20 m. The coarse grid developed for Area C extends approximately 12 km offshore and 51 km alongshore. Depths at the offshore boundary vary between 14 and 44 m (NGVD), with a mean depth of approximately 21 m. Finally, the coarse grid developed for Area D extends approximately 9 km offshore and 36 km alongshore. Depths at the offshore boundary vary between 18 and 138 m (NGVD), with a mean depth of approximately 47 m.

Table 4-3. Input wave spectra parameters used for existing and post-dredging STWAVE runs for modeled Area C.

	STWAVE Model Input Condition	Percent Occurrence	H _{mo} Wave Height (m)	Peak Wave Period, T _p (sec)	Peak Wave Direction, θ _p (° true north)	Peak Wave Direction, θ _p (grid relative)	Direction Bin (grid relative)
Period Band 1	1C	4.5	1.6	6.8	32	55	33.75-56.25
	2C	12.3	1.5	7.5	47	70	56.25-78.75
	3C	7.2	1.4	7.5	72	95	78.75-90.00
	4C	8.4	1.2	7.4	67	90	90.00-101.25
	5C	11.5	1.0	6.9	87	110	101.25-123.75
	6C	4.5	1.1	5.4	107	130	123.75-146.25
Period Band 2	7C	18.4	1.4	12.3	52	75	56.25-78.75
	8C	11.9	1.5	14.0	62	85	78.75-90.00
	9C	7.5	1.4	12.1	67	90	90.00-101.25
	10C	2.0	1.1	11.1	87	110	101.25-123.75

Table 4-4. Input wave spectra parameters used for existing and post-dredging STWAVE runs for modeled Area D.

	STWAVE Model Input Condition	Percent Occurrence	H _{mo} Wave Height (m)	Peak Wave Period, T _p (sec)	Peak Wave Direction, θ _p (° true north)	Peak Wave Direction, θ _p (grid relative)	Direction Bin (grid relative)
Period Band 1	1D	7.0	1.4	6.9	32	50	33.75-56.25
	2D	15.3	1.3	7.4	47	65	56.25-78.75
	3D	10.8	1.2	7.3	67	85	78.75-90.00
	4D	3.3	1.3	5.8	77	95	90.00-101.25
	5D	5.9	1.2	5.5	92	110	101.25-123.75
	6D	4.1	1.1	4.9	117	135	123.75-146.25
PB 2	7D	24.5	1.3	12.9	57	75	56.25-78.75
	9D	12.6	1.3	13.0	62	80	78.75-90.00

Post-dredging coarse grids were developed by imposing modifications to the existing conditions bathymetry; Table 4-6 presents the resource characteristics of modeled borrow sites. For each site, bathymetry was excavated to the indicated depth. Bathymetry deeper than the excavated depth was not modified. For each modeled area, the same fine grid was used for existing conditions and post-dredging simulations. Spatially varying boundary conditions (wave spectra) for fine grids were extracted from coarse grid simulations. As such, the fine grid solution was nested within the coarse grid solution.

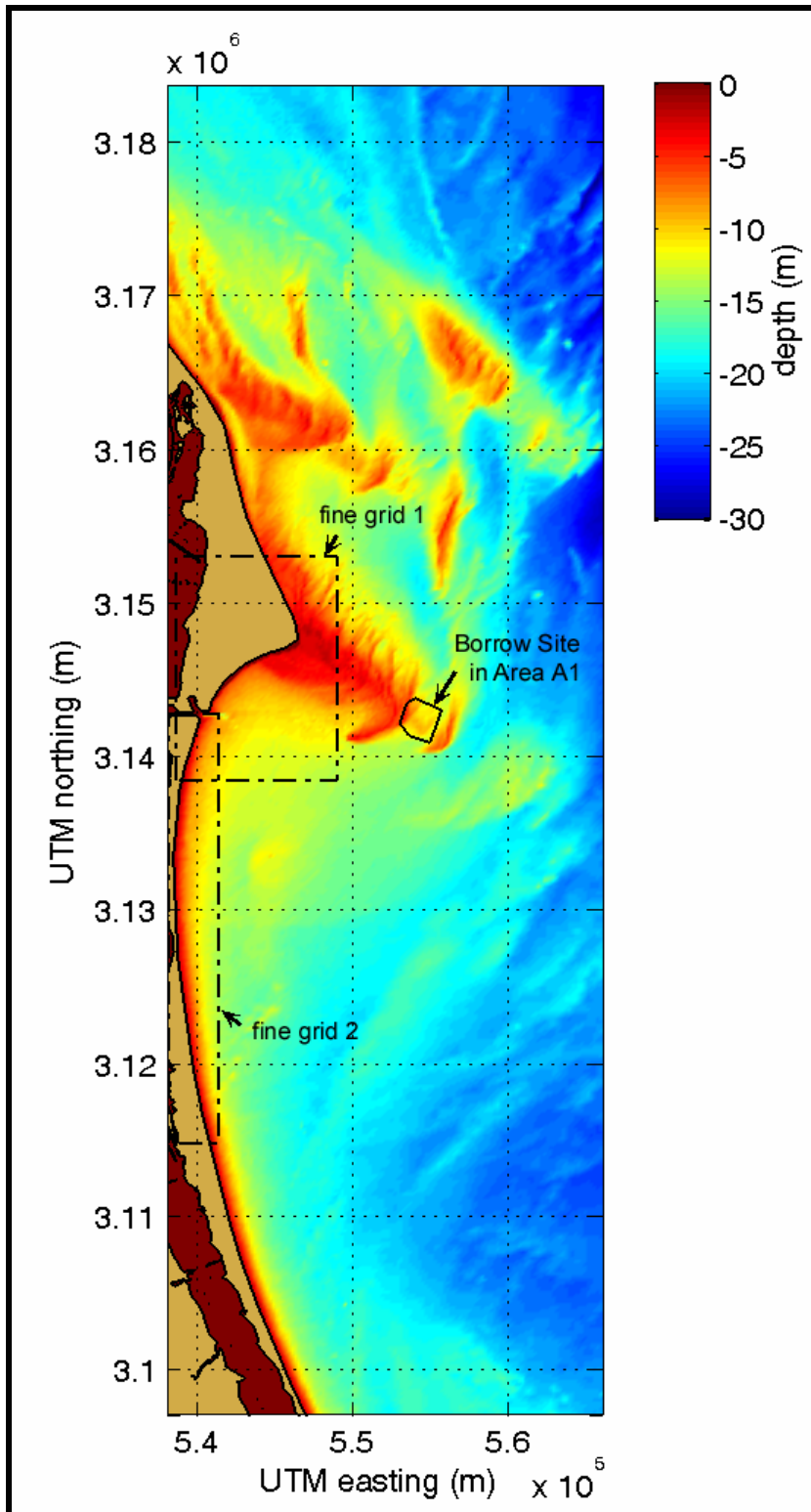


Figure 4-9. Coarse model grid (200 x 200 m spacing) used for STWAVE simulations offshore Cape Canaveral, FL. Depths are relative to NGVD. Borrow site location is indicated by the solid black line, and fine grid limits are indicated by a dashed line.

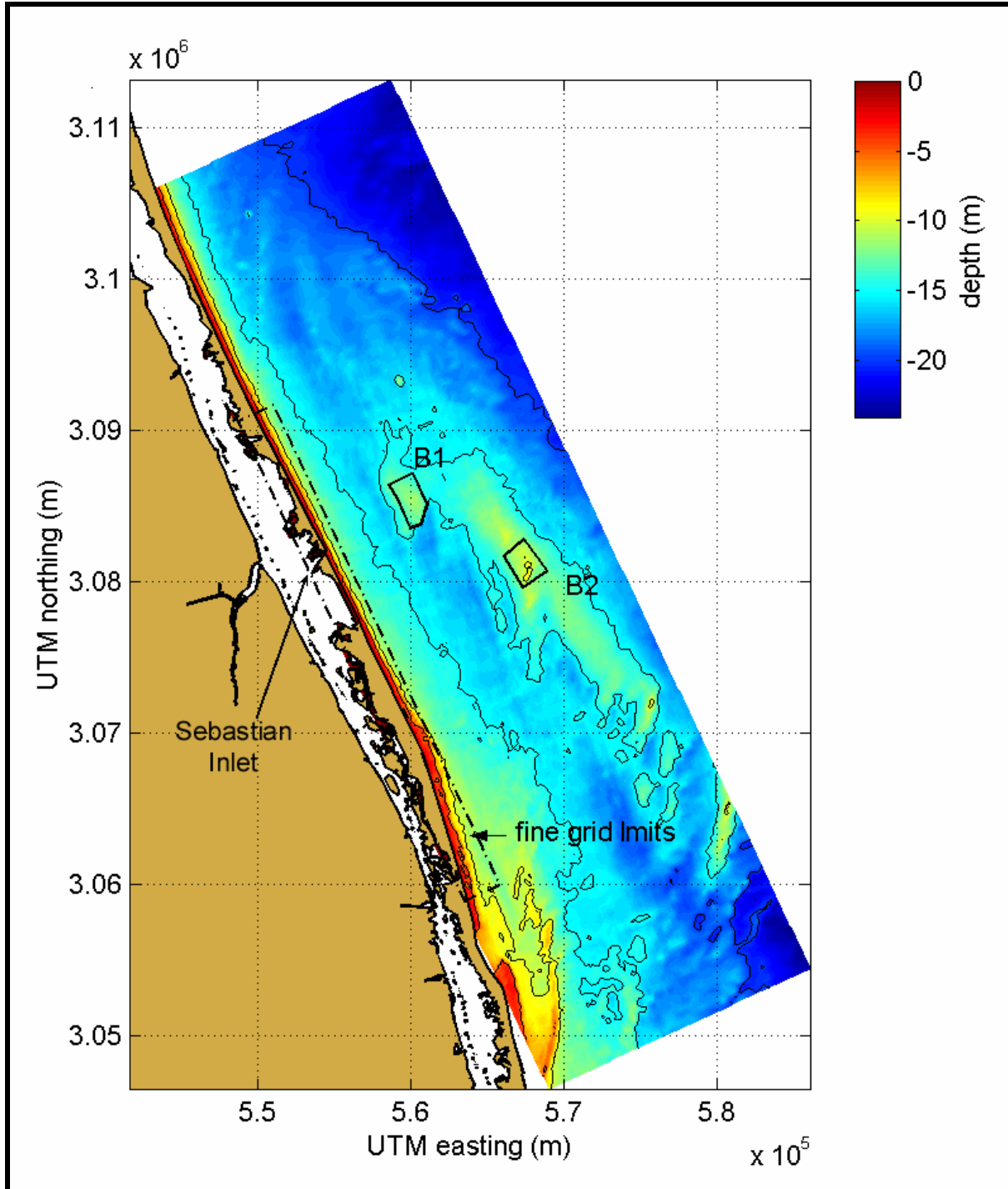


Figure 4-10. Coarse model grid (200 x 200 m spacing) used for STWAVE simulations offshore Sebastian Inlet, FL. Depths are relative to NGVD. Borrow site locations are indicated by solid black lines, and fine grid limits are indicated by a dashed line. B1 is the borrow site in Sand Resource Area B1, and B2 is the borrow site in Sand Resource Area B2.

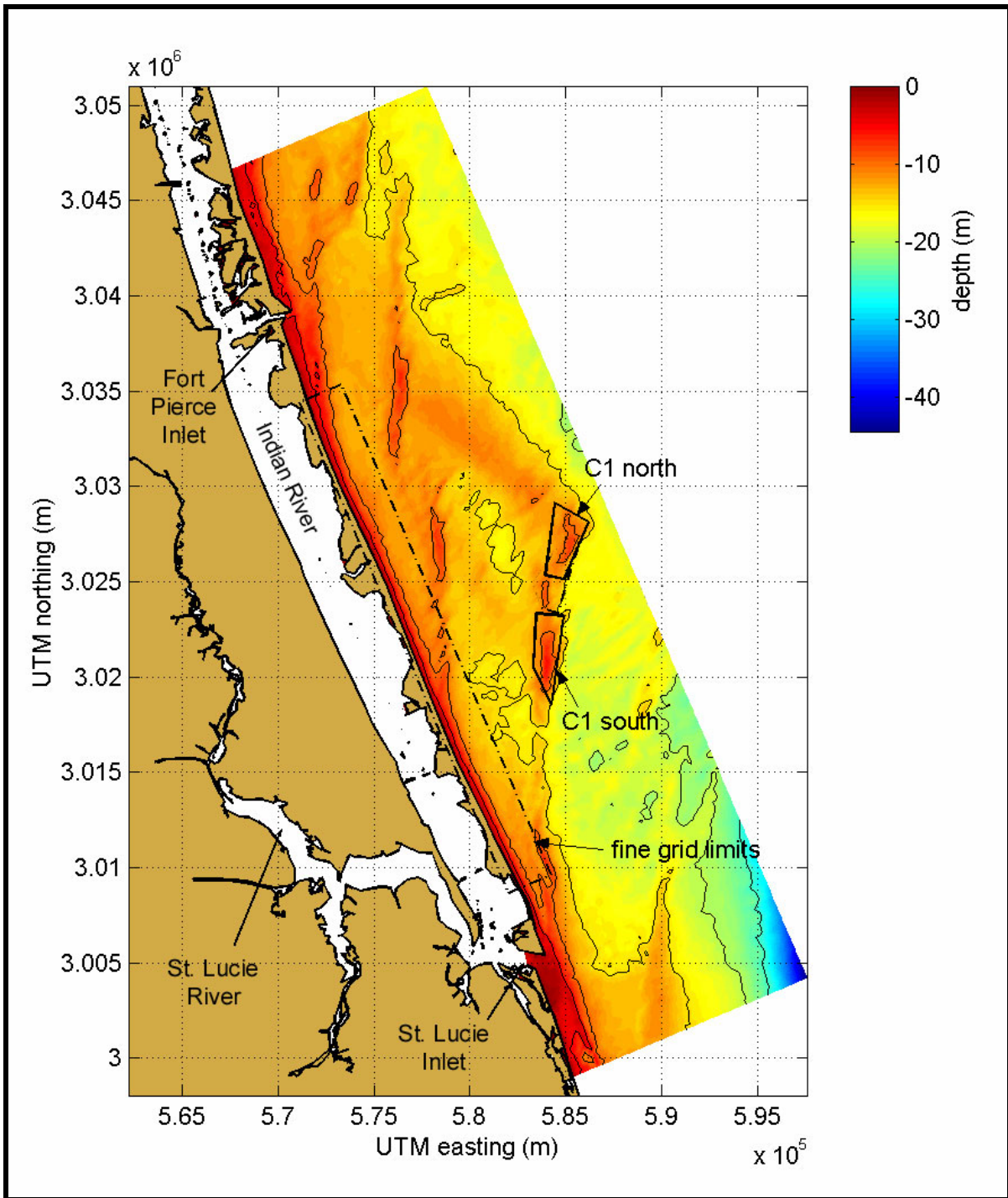


Figure 4-11. Coarse model grid (200 x 200 m spacing) used for STWAVE simulations offshore St. Lucie Inlet, FL. Depths are relative to NGVD. Borrow site locations are indicated by solid black lines, and fine grid limits are indicated by a dashed line. C1 north is the northern borrow site in Sand Resource Area C1, and C1 south is the southern borrow site in Sand Resource Area C1.

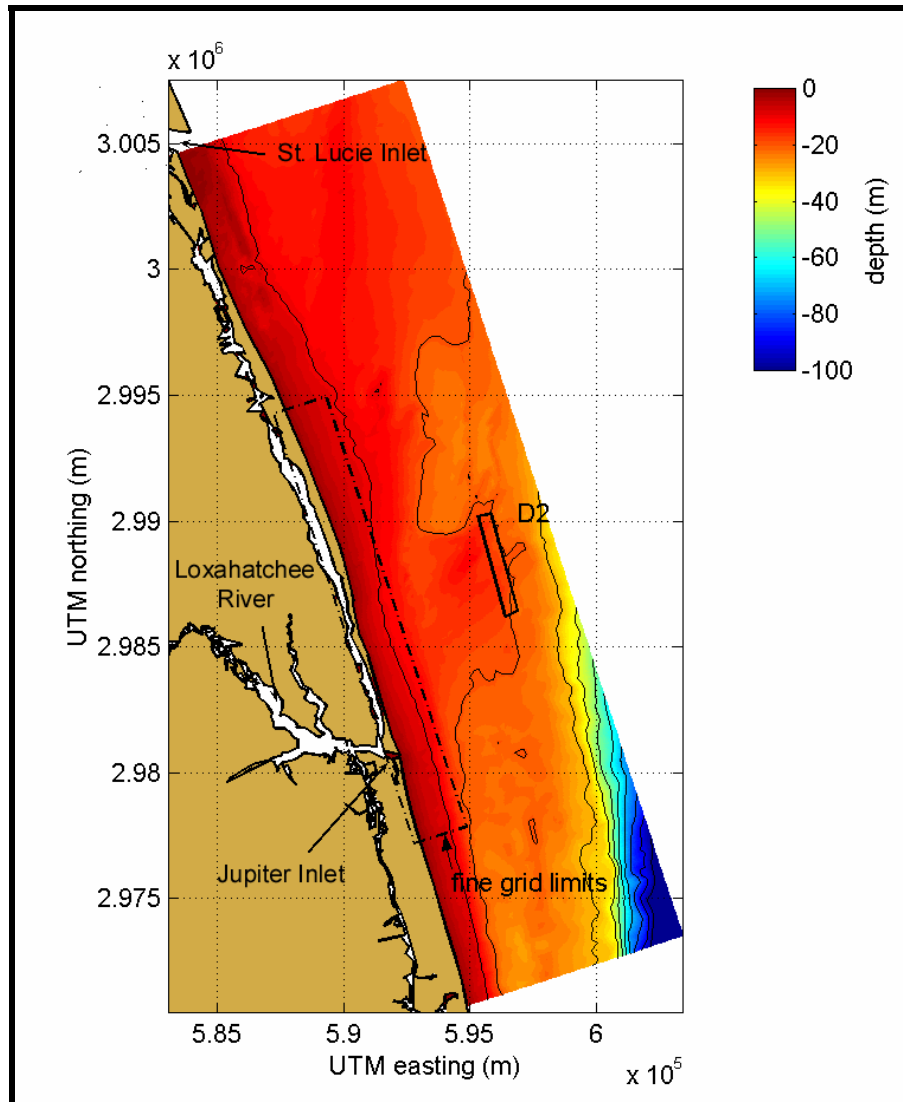


Figure 4-12. Coarse model grid (200 x 200 m spacing) used for STWAVE simulations offshore Jupiter Inlet, FL. Depths are relative to NGVD. Borrow site locations are indicated by solid black lines, and fine grid limits are indicated by a dashed line. D2 is the borrow site that extends from Sand Resource Area D1 into Sand Resource Area D2 along the Federal-State boundary.

Table 4-5. Numerical grid dimensions for offshore (coarse) and nearshore (fine) grids. Dimensions are given as cross-shore x alongshore.

Region	Coarse Grid (200 m spacing)		Fine Grid (20 m spacing)		Grid Angle (° true north)
	Nodes	Distance (km)	Nodes	Distance (km)	
Area A	141 x 434	28 x 87	520 x 730	10 x 15	0
			160 x 1400	3 x 28	
Area B	95 x 325	19 x 65	13 1 x 1751	2.6 x 35	-25
Area C	70 x 255	14 x 51	121 x 1401	2.4 x 28	-23
Area D	50 x 180	10 x 36	111 x 901	2.2 x 18	-18

Table 4-6. Sand resource characteristics at potential borrow sites in resource areas offshore central east Florida.						
Resource Area	Borrow Site Surface Area (x 10 ⁶ m ²)	Maximum Excavation Depth (m)	Borrow Site Sand Volume (x 10 ⁶ m ³)	D10 (mm)	D50 (mm)	D90 (mm)
A1	5.39	12	13.6	0.70	0.32	0.21
B1	4.62	15	11.0	1.15	0.60	0.28
B2	3.48	13	7.6	1.49	0.47	0.25
C1 north	5.16	12	5.8	1.96	0.61	0.26
C1 south	4.71	12	8.8	0.62	0.29	0.18
D2	2.25	20	4.1	0.59	0.31	0.20

D10 = grain diameter above which 10% of the distribution is retained; D50 = median grain diameter; D90 = grain diameter above which 90% of the distribution is retained.

4.1.2 Sediment Transport Potential

As a first step in evaluating sediment transport along the coastline of central east Florida, calculations of sediment transport potential were performed to indicate the maximum quantity of sand transport possible based on a sediment-rich environment. Results from the spectral wave modeling formed the basis for quantifying changes in sediment transport rates along the beach because wave-induced transport is a function of wave breaker height, wave period, and wave direction. Longshore transport depends on long-term fluctuations in incident wave energy and the resulting longshore current; therefore, annual transport rates were calculated from long-term wave statistics.

The sediment transport equation used for longshore analyses is based on work of the Rosati et al. (2002). In general, the longshore sediment transport rate is assumed to be proportional to the longshore wave energy flux at the breaker line, which is dependent on wave height and direction. Because the transport equation was calibrated in sediment-rich environments, it typically over-predicts sediment transport rates. However, it provides a useful technique for comparing erosion/accretion trends along a shoreline of interest.

Sediment transport computations were based on wave information at breaking for each grid cell along the modeled coastline. This shoreline segment incorporates the influence of all changes to the nearshore wave climate associated with proposed dredging activities. Computations of sediment transport rates for each wave condition was performed and then weighted by the annual percentage occurrence. Sediment transport potential was computed for existing and post-dredging conditions with the equations described in Appendix B.

4.2 MODEL RESULTS

Redistribution of wave energy and alteration of wave directions resulting from offshore sand excavation are expected to change longshore sediment transport patterns landward of potential sand borrow sites in central east Florida. Depending on the net direction of local sediment transport, the influence of borrow site conditions can either increase or decrease net littoral drift. Example model cases for each potential sand borrow site offshore central east Florida are discussed in the following subsections. Complete results for the four modeled regions, showing wave heights and wave height difference plots between existing and post-dredging conditions for all modeled wave cases, is provided in Appendix C.

4.2.1 Wave Modeling

From existing conditions model results, bottom features offshore central east Florida modified the wave field as it propagated shoreward. As an example, the shoal in the vicinity of Borrow Sites C1 north and C1 south (approximately 7 m water depth) refracts and focuses wave energy, resulting in an area of increased wave heights shoreward of the shoal (Figure 4-13). Wave heights landward of the shoal were about 0.3 m greater than wave heights seaward of the shoal. As the shoal focused wave energy and caused an increase in wave height in one area, there was a corresponding decrease in wave energy in adjacent areas. Because energy was conserved, wave focusing behind the shoal caused a reduction of energy at the southern edge of the shoal, which is illustrated by reduced wave heights.

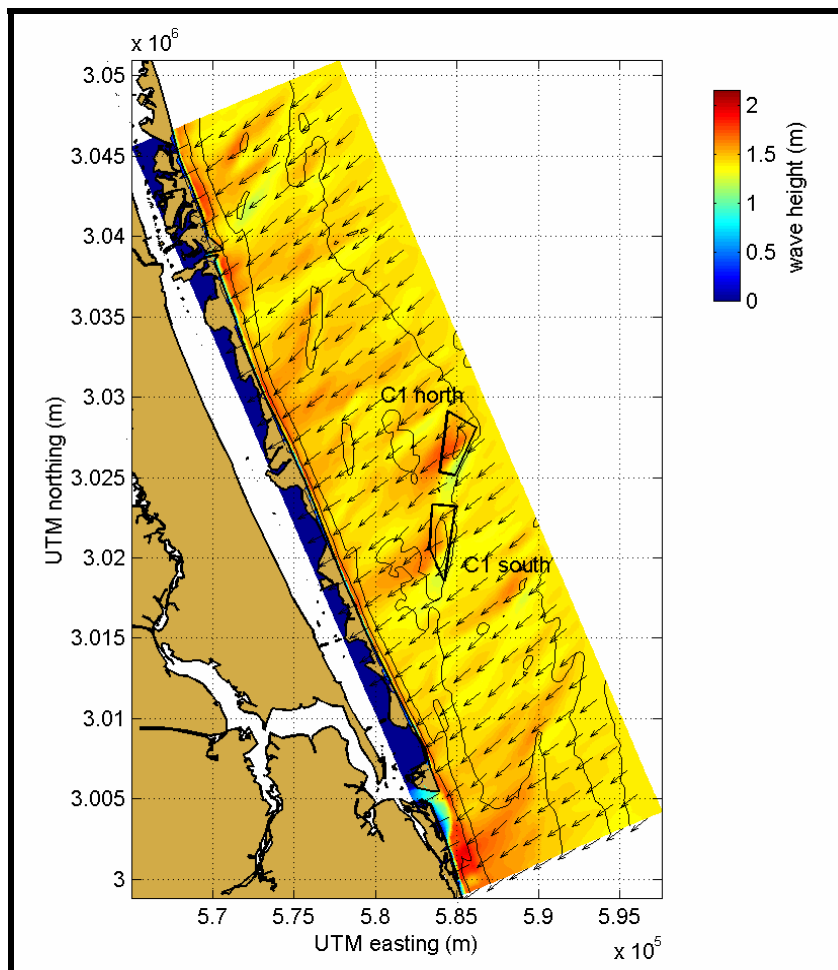


Figure 4-13. STWAVE output for the coarse grid in wave modeling Area C (200 x 200 m grid cells) offshore St. Lucie Inlet ($H_{m0} = 1.4$ m, $T_p = 12.3$ sec). Color contours indicate H_{m0} wave height. Vectors indicate mean wave direction. Seafloor contours are shown at 5 m intervals.

In addition to the effects of bottom features far offshore, waves were refracted by straight and parallel bottom contours in the nearshore. In Figure 4-14, fine grid model results illustrate how wave directions changed as the wave field propagates shoreward. For the same northeast wave condition as in Figure 4-13, waves refracted and the mean direction of wave propagation near the shoreline became shore-normal (perpendicular to the

shoreline). In addition to the change in wave direction, wave heights also were modified by nearshore bathymetry. Waves began to shoal (increase in height) about 400 m offshore and increased in height by 0.2 m before breaking began. Wave heights were reduced as energy was dissipated in the surf zone, which was about 120 m wide in this example.

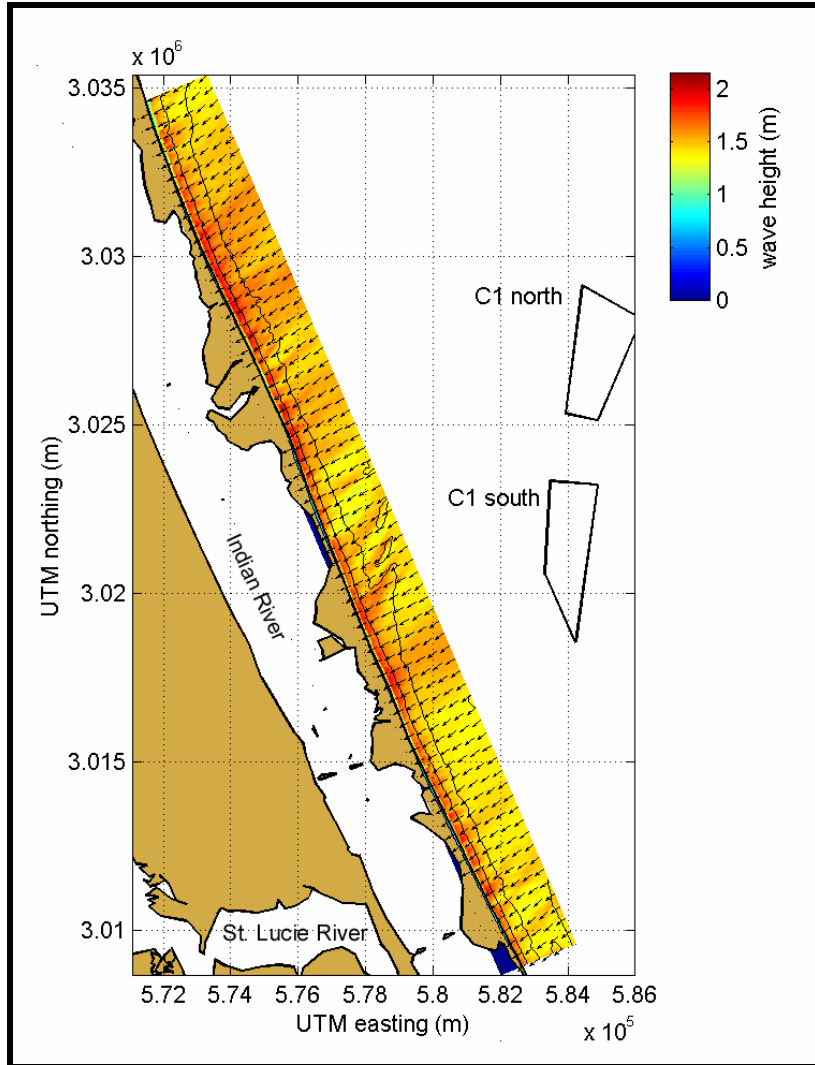


Figure 4-14. STWAVE output for the fine grid in wave modeling Area C (20 x 20 m grid cells) offshore St. Lucie Inlet ($H_{m0} = 1.4$ m, $T_p = 12.3$ sec). Color contours indicate H_{m0} wave height. Vectors indicate mean wave direction. Seafloor contours are shown at 5 m intervals.

Overall, post-dredging wave model output illustrated reduced wave heights landward of borrow sites and increased wave heights at the longshore limits of each borrow site. As waves propagated across a borrow site (deeper water than the surrounding area), wave refracted away from the center of the borrow site and toward the shallower edges. The net effect was to create a shadow zone of reduced wave energy immediately landward of a borrow site and a zone of increased wave energy updrift and downdrift of a borrow site.

This shadowing effect was apparent in the wave height difference plot presented in Figure 4-15. Color contours represent wave height differences between model results computed for existing and post-dredging conditions. For this particular wave case, there

was an obvious interaction between the two borrow sites, as Site C1 south fell within the influence of Site C1 north (i.e., C1 south is in the shadow zone of C1 north). Not all wave cases for this modeled area exhibited this same overlapping influence. Maximum wave height reduction occurred landward of Site C1 south, where wave heights were reduced by 0.2 m. The areas of greatest wave height increase were found along the southeastern edges of both sites, where wave heights increased 0.9 m over existing conditions.

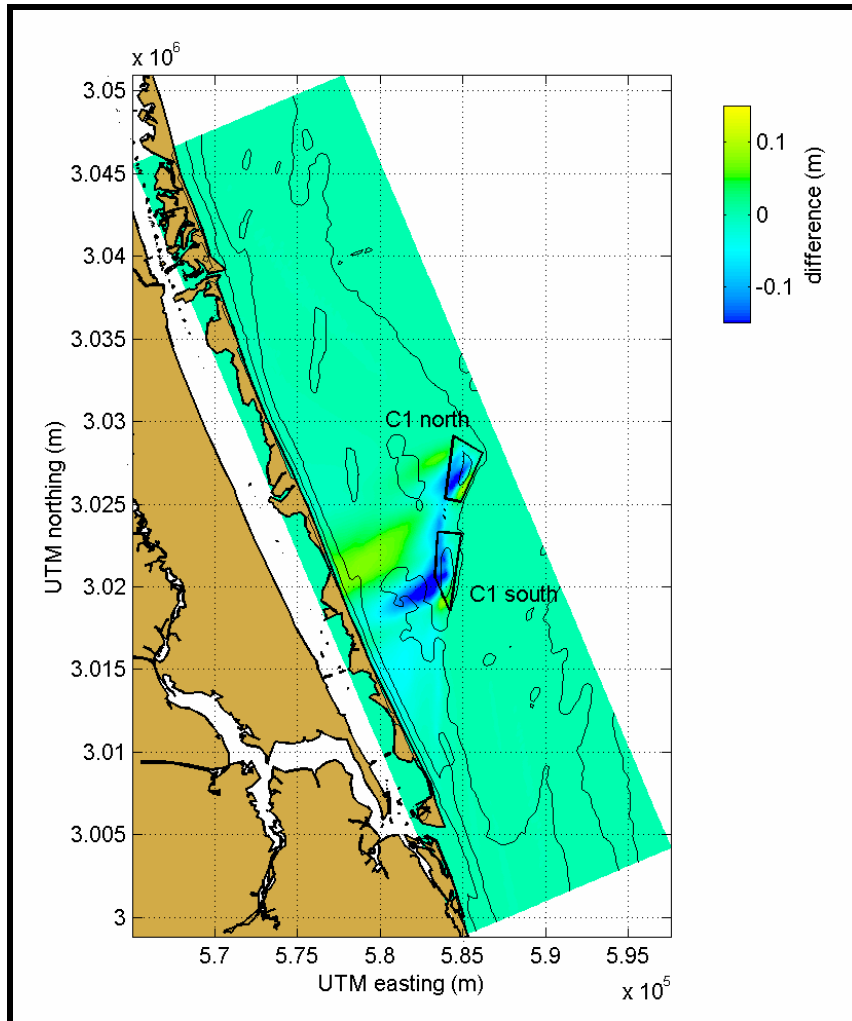


Figure 4-15. Wave height difference plot ($H_{\text{difference}} = H_{\text{post}} - H_{\text{existing}}$) for coarse grid model for St. Lucie Inlet. Seafloor contours are shown at 5 m intervals.

Because these are spectral wave model results, and because different frequencies in the spectrum are refracted by varying degrees at the borrow sites, areas of increased and reduced wave height gradually diffuse as the wave field approaches shore. This resulted in smaller changes in wave heights close to the shoreline (Figure 4-16). Another result of the energy diffusion process was that the length of shoreline affected by a borrow site (or combination of borrow sites) can be considerably longer than the borrow site. In Figure 4-16, the length of affected shoreline was approximately three times longer than the alongshore limits of the two borrow sites (i.e., the north corner of Site C1 north and the south corner of Site C1 south).

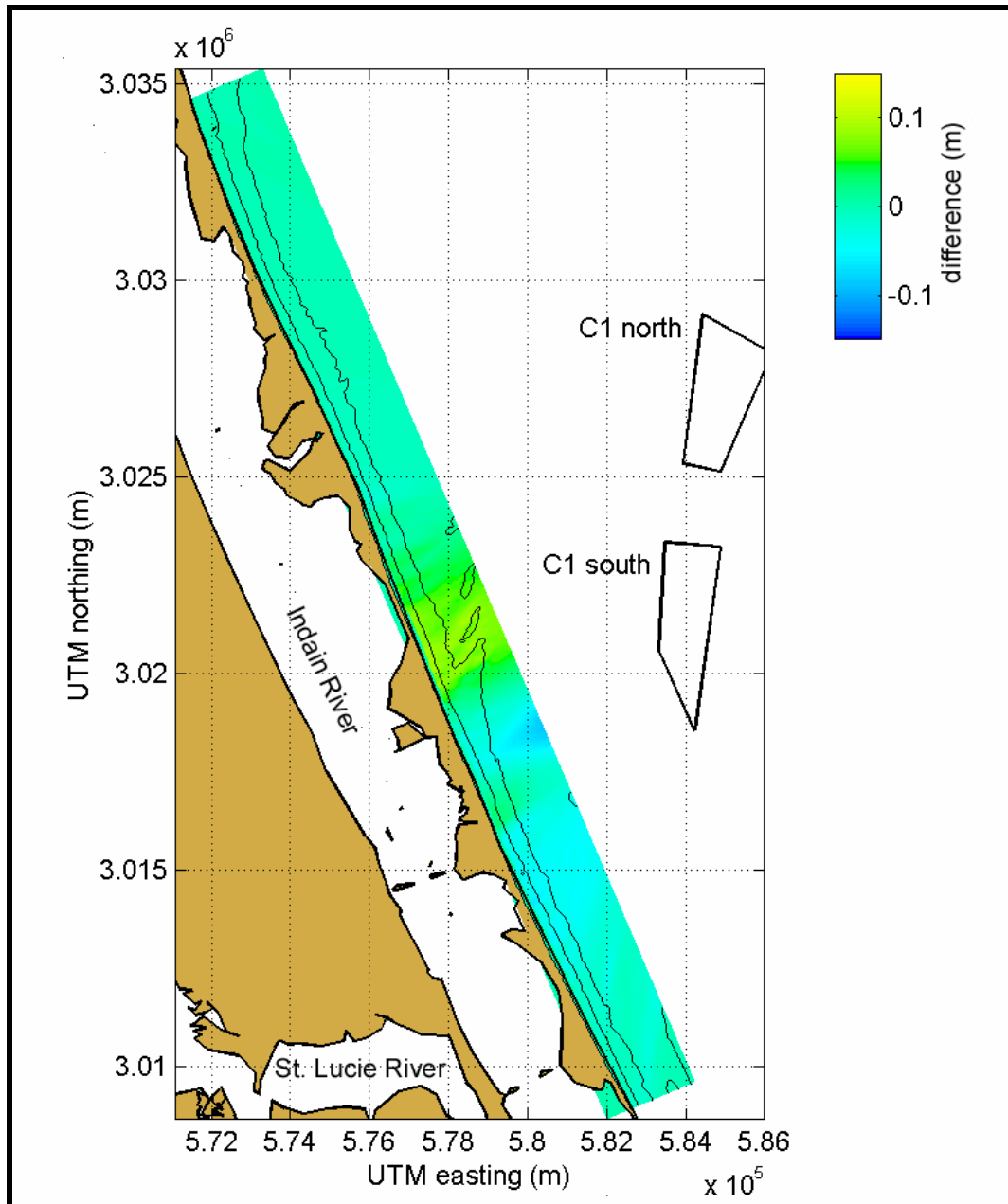


Figure 4-16. Wave height difference plot for fine grid model simulations offshore St. Lucie Inlet. Seafloor contours are shown at 5 m intervals.

4.2.1.1 Area A

Model output for existing conditions simulations offshore Cape Canaveral for wave Case 3A (Table 4-1) is presented in Figure 4-17. Canaveral Shoals, the complex of ridges and troughs that extend southeast from Cape Canaveral, caused significant increases in wave height as waves propagated over this area. As waves refracted around the shoals, wave heights increased by 0.5 m over offshore wave conditions. In the shoal field northeast of the Cape, wave heights increased by about 0.3 m above offshore wave heights. Wave direction changes also were observed in these areas.

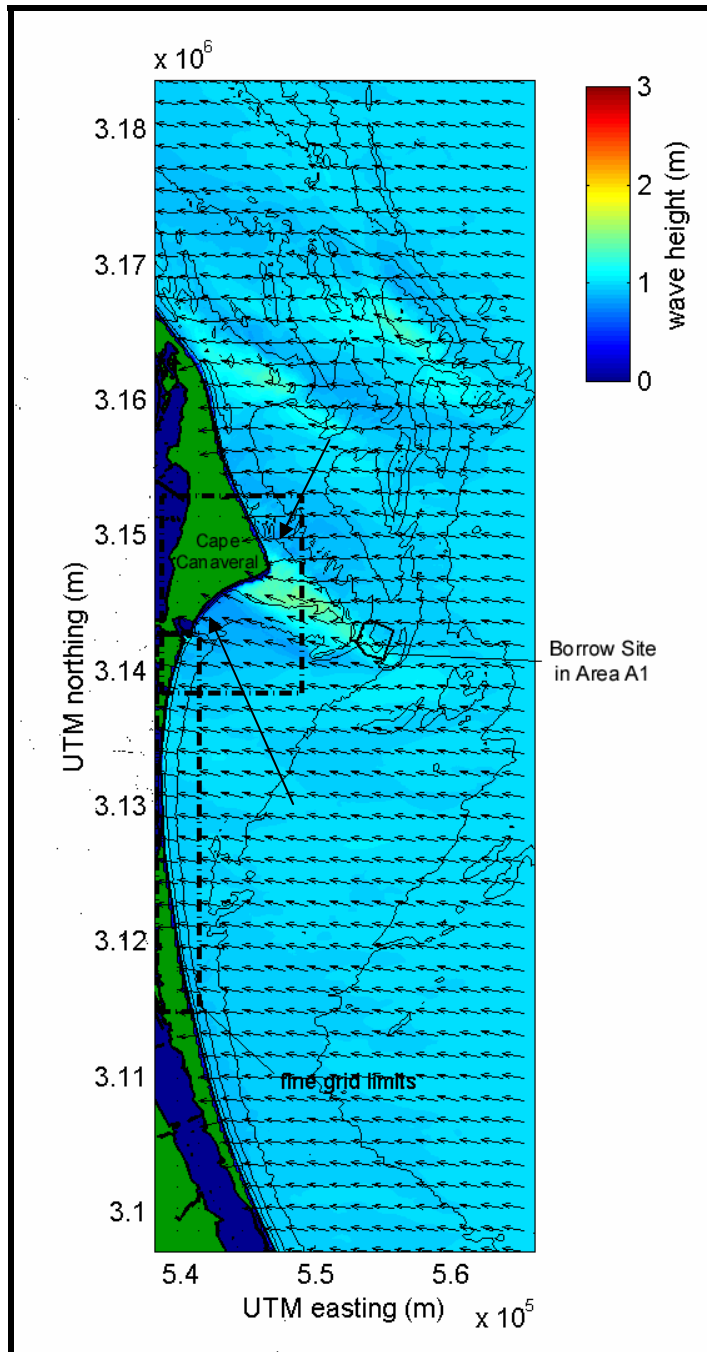


Figure 4-17. STWAVE output for wave modeling Area A, wave Case 3A ($H_s = 1.0$ m, $T_{peak} = 7.7$ sec, $\theta_{peak} = 100$ deg). Color contours indicate wave height, and vectors show mean direction of wave propagation. Seafloor contours are shown at 5 m intervals.

A greater degree of wave refraction was illustrated in model output for Case 6A (Figure 4-18). The offshore condition was a 1.6 m, 14.3 sec wave propagating from the east-northeast.

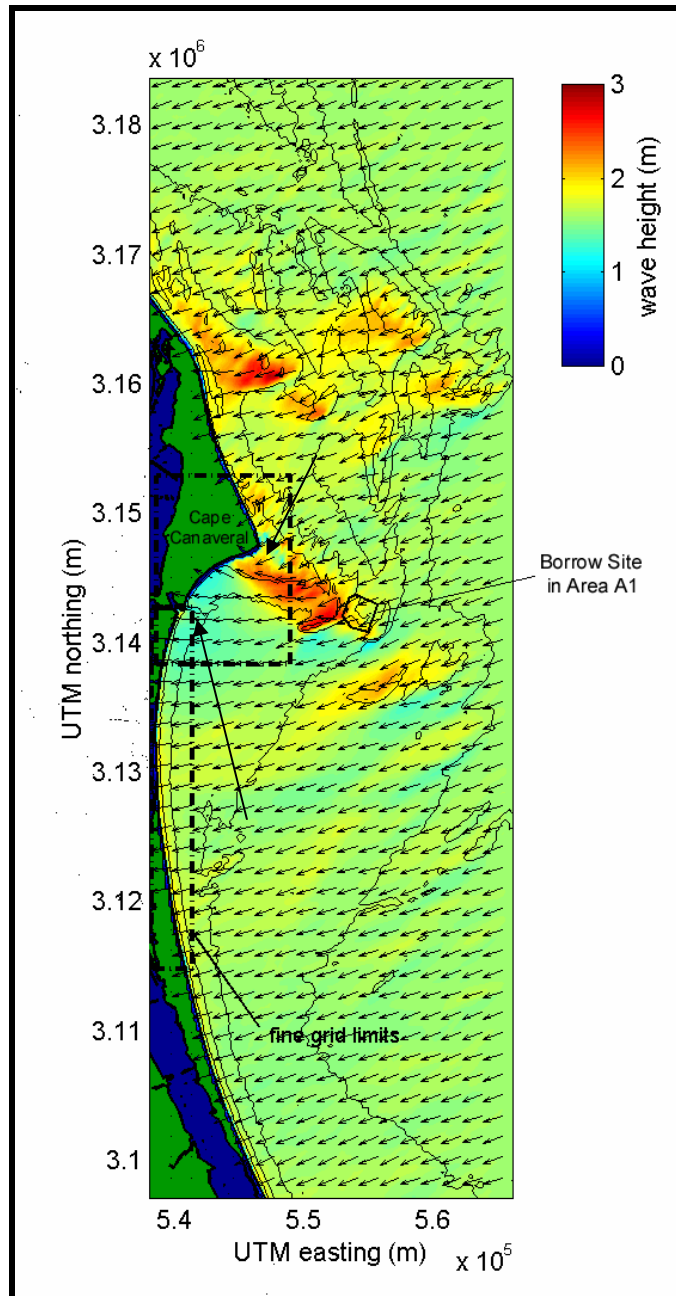


Figure 4-18. STWAVE output for wave modeling Area A, wave Case 6A ($H_s = 1.6$ m, $T_{peak} = 14.3$ sec, $\theta_{peak} = 65$ deg). Color contours indicate wave height, and vectors show mean direction of wave propagation. Seafloor contours are shown at 5 m intervals.

Vectors indicating wave direction illustrated that for some nearshore regions adjacent to the Cape, the direction of wave propagation changed more than 45 degrees, following the gradient in bathymetric contours. Largest waves in the model domain occurred at the shoals north of Canaveral Harbor (1.3 m higher than offshore waves). At shoals in the vicinity of the borrow site in Area A1, wave heights increased to a maximum of 2.8 m, 1.2 m above offshore conditions. Shoals tended to refract wave energy and caused focusing (wave convergence) near the Cape. However, the coast south of the Cape illustrated reduced wave heights (wave divergence).

Post-dredging wave height changes are illustrated in Figures 4-19 and 4-20 for Cases 3A and 6A, respectively. For Case 3A, maximum wave height increase resulting from dredging the borrow site was 0.2 m, and the maximum decrease in the shadow zone of the site was 0.3 m. The overall area of influence for this borrow site extended approximately 14 km north of the Cape to about 4 km south of Canaveral Harbor.

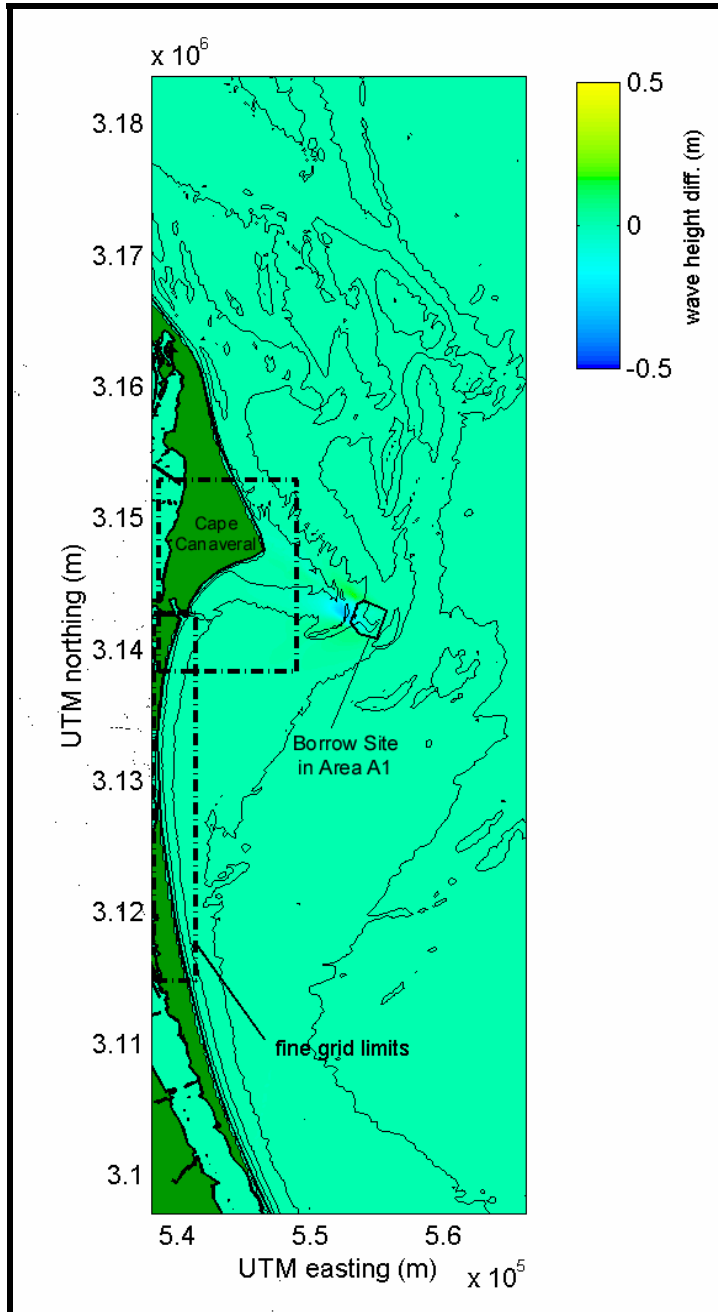


Figure 4-19. Wave height change between existing and post-dredging conditions at wave modeling Area A for STWAVE simulations, wave Case 3A ($H_s = 1.0$ m, $T_{peak} = 7.7$ sec, $\theta_{peak} = 100$ deg). Seafloor contours are shown at 5 m intervals.

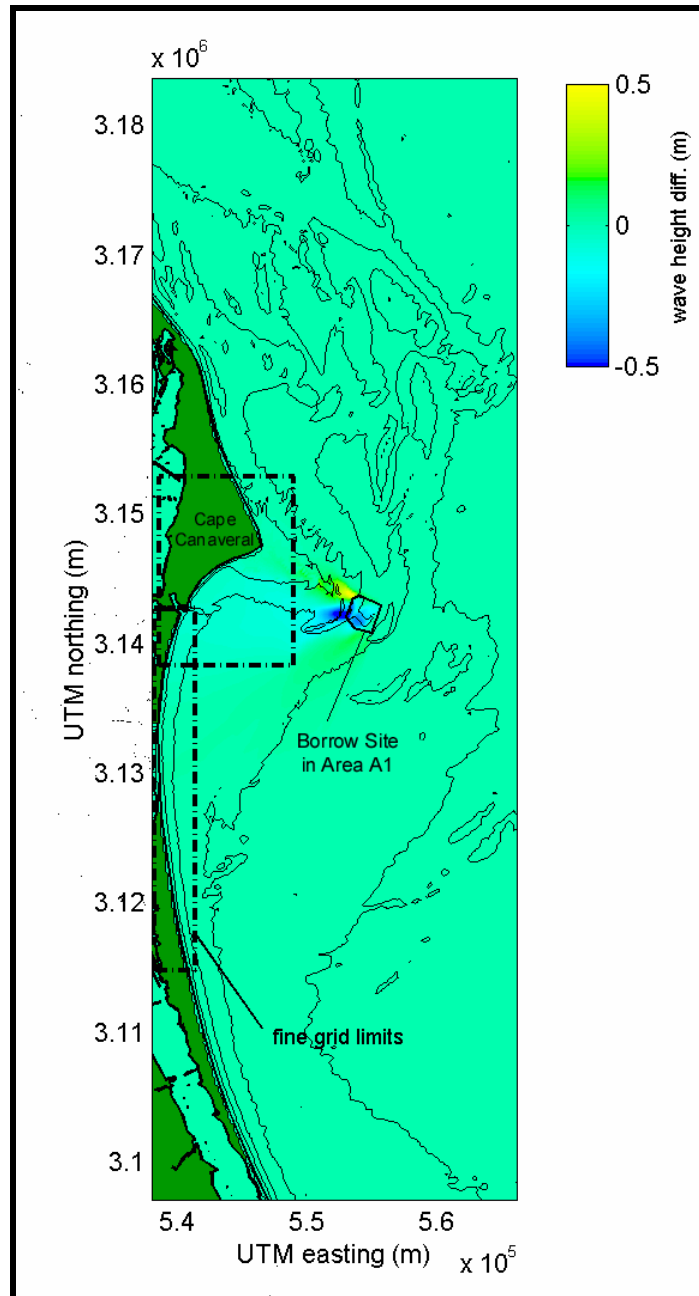


Figure 4-20. Wave height change between existing and post-dredging conditions at wave modeling Area A for STWAVE simulations, wave Case 6A ($H_s = 1.6$ m, $T_{peak} = 14.3$ sec, $\theta_{peak} = 65$ deg). Seafloor contours are shown at 5 m intervals.

Similar wave difference results were illustrated for Case 6A (Figure 4-20). Maximum change in post-dredging wave heights was 0.7 m, substantially greater than change observed at other sites. The area of greatest wave height increase occurred at the northwest corner of the site. Wave heights did not increase by the same amount at the southwest corner, likely due to local bathymetry and geometry of the site. Deeper excavation depths at the northwest corner cause a greater degree of wave refraction. The longshore extent of influence was similar to that of Case 3A, but its location shifted slightly southward due to the direction of wave propagation.

4.2.1.2 Area B

Wave model output for offshore Sebastian Inlet at borrow sites in Areas B1 and B2 are illustrated in Figures 4-21 through 4-24. Figure 4-21 shows coarse grid results for wave Case 1B, a 1.9 m, 6.9 sec wave propagating from the NNE. Based on WIS results, waves from this direction occurred 2.3% of the time. For this relatively short period wave case, offshore bathymetry had a limited effect on the wave field as it propagated shoreward. The shoal encompassing the borrow site in Area B1 had the greatest influence on wave propagation in the region, although effects were small because the shoal had a minimum depth of approximately 12 m NGVD. Results from wave Case 10B are illustrated in Figure 4-22. This case had a similar wave height but longer peak period ($H_s = 1.7$ m, $T_{peak} = 10.8$ sec) than Case 1B. As such, wave refraction was greater and the influence of bottom features, like the shoal in Area B1, was more pronounced. Wave heights shoreward of the shoal were approximately 0.2 m greater than wave heights seaward of the feature.

Changes in the wave field caused by dredging at borrow sites in Areas B1 and B2 are shown for wave Cases 1B and 10B in Figures 4-23 and 4-24. To simulate borrow site dredging, bathymetry within each of the designated areas was lowered to an isobathic level. In effect, shoal relief was leveled to a constant elevation within each borrow site. Generally, less material was removed from the periphery of the site boundaries, and deeper dredging occurred near the center of the site. The difference plot in Figure 4-23 was computed by subtracting waves heights computed for existing conditions from those computed for post-dredging conditions. Therefore, negative differences indicated areas where wave height decreased after dredging occurred, and positive differences showed areas of increased height after dredging.

For wave Case 1B, borrow sites had a limited influence on waves over a long section of coast (>30 km), but changes on the order of 0.01 m occurred along 2.5 km of coast landward of the borrow site in Area B1 (Figure 4-23). At this borrow site, maximum change in wave height was approximately 0.10 m. Maximum change in wave height was approximately 0.12 m at the borrow site in Area B2. Even though the borrow site in Area B2 was smaller than that in Area B1 (i.e., less sediment dredged), B2 had a slightly greater impact on local wave heights. This apparent paradox is due to subtle changes in bathymetry relative to borrow site geometry.

The wave difference plot computed for wave Case 10B illustrates that changes to the wave field resulting from dredging at sand borrow sites in Areas B1 and B2 were more pronounced than for wave Case 1B (Figure 4-24). The length of shoreline influenced by changes in wave propagation from the two borrow sites was approximately 20 km; however, greatest changes (about 0.01 m) occurred within a 12 km stretch of coast. The zone of influence for this wave case illustrated two regions of increased wave height propagating from the lateral boundaries of the sites and a single zone of reduced heights at the shoreward boundaries. At B1, maximum changes in wave height were 0.13 m, very similar to those computed for the borrow site in Area B2. Although the magnitude of maximum wave height change for wave Case 10B was slightly larger than 1B, shoreline impacts associated with 10B were greater. Longer period waves of Case 10B were affected more by bathymetry in deeper water, causing larger areas of waves on the shoals to be impacted by dredging changes at borrow sites. This process resulted in a broader area of impacted shoreline.

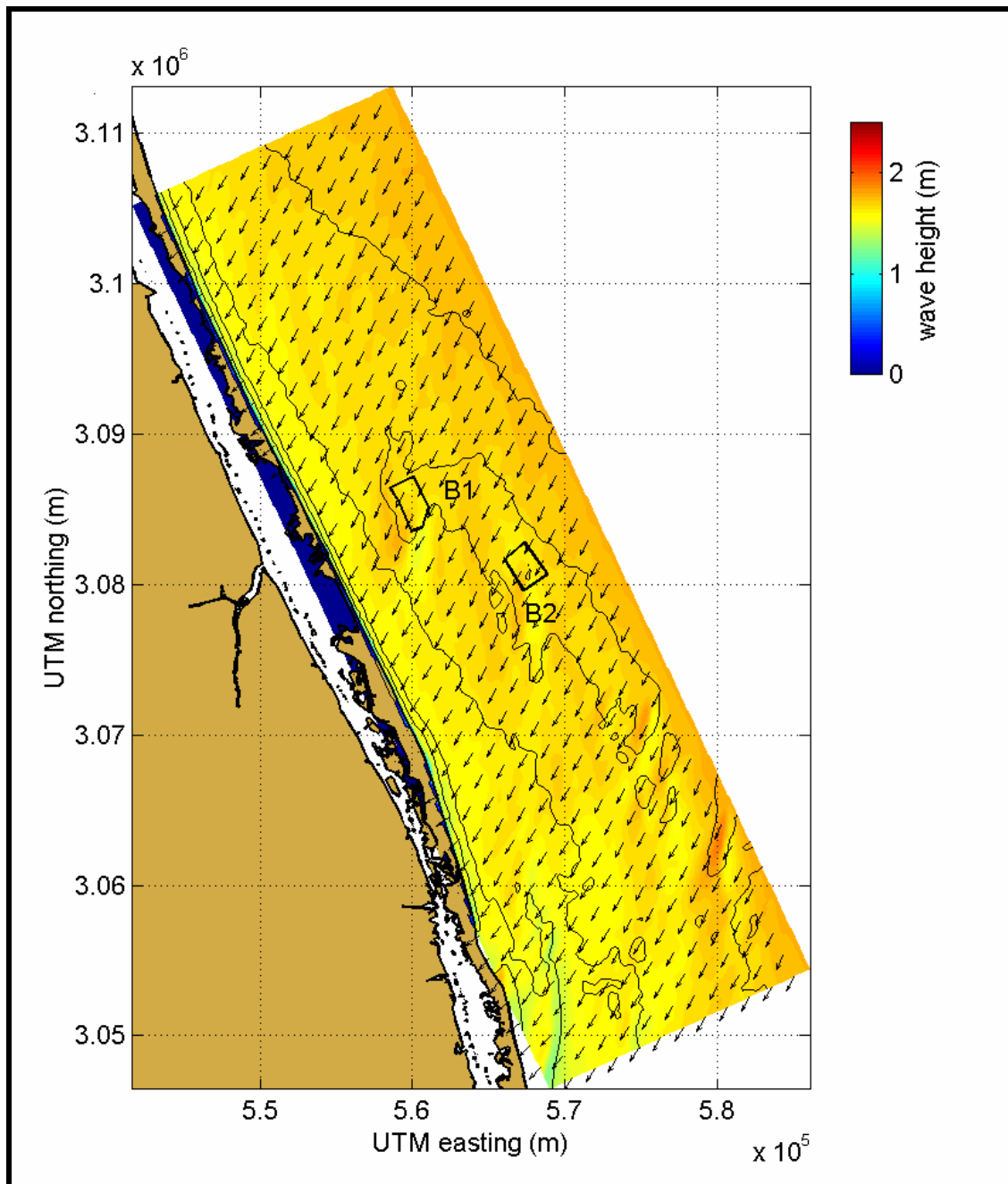


Figure 4-21. STWAVE output for wave modeling Area B, wave Case 1B ($H_s = 1.9$ m, $T_{peak} = 6.9$ sec, $\theta_{peak} = 25$ deg). Color contours indicate wave height, and vectors show mean direction of wave propagation. Seafloor contours are shown at 5 m intervals. B1 is the borrow site in Sand Resource Area B1, and B2 is the borrow site in Sand Resource Area B2.

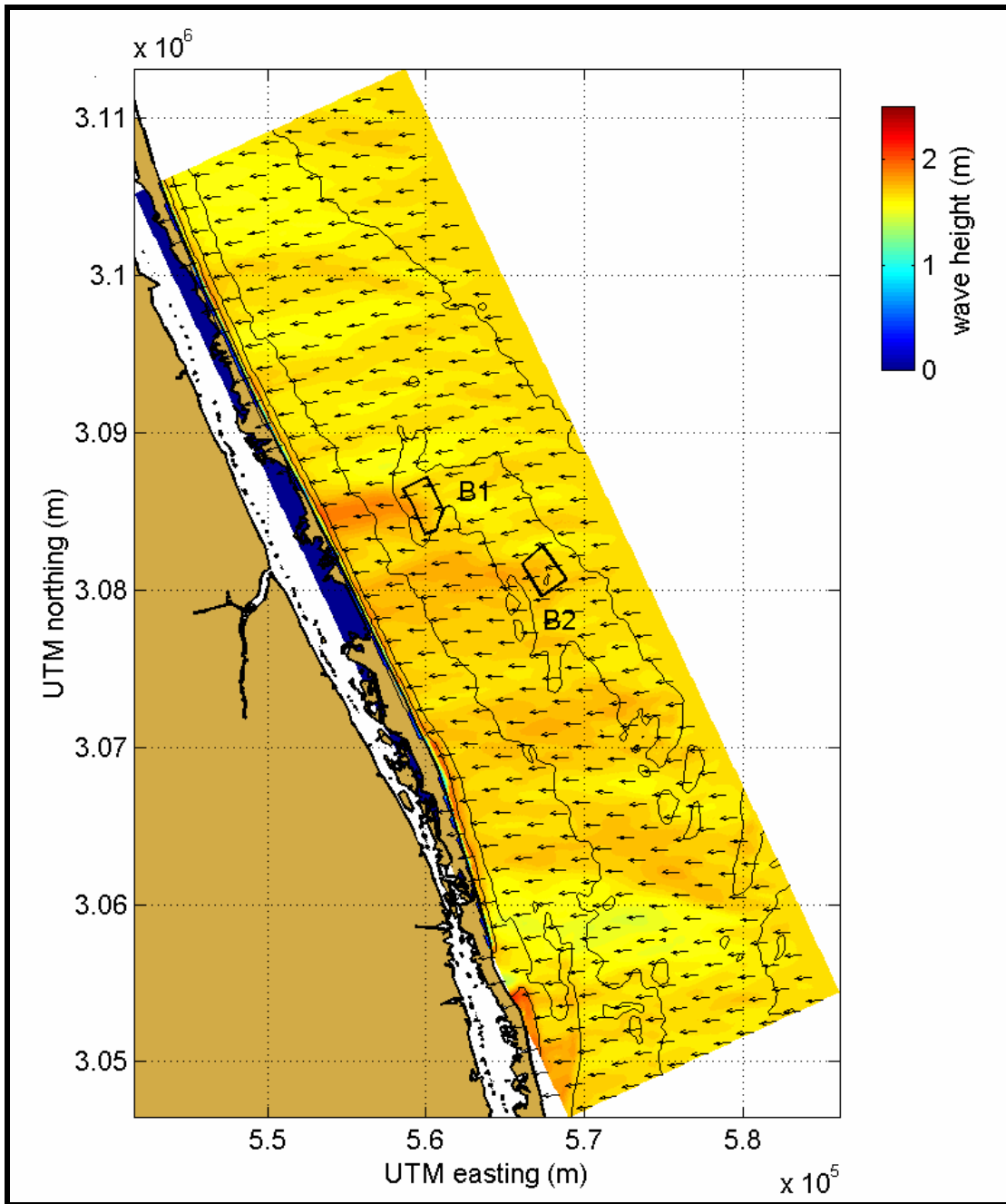


Figure 4-22. STWAVE output for wave modeling Area B, wave Case 10B ($H_s = 1.7$ m, $T_{peak} = 10.8$ sec, $\theta_{peak} = 90$ deg). Color contours indicate wave height, and vectors show mean direction of wave propagation. Seafloor contours are shown at 5 m intervals. B1 is the borrow site in Sand Resource Area B1, and B2 is the borrow site in Sand Resource Area B2.

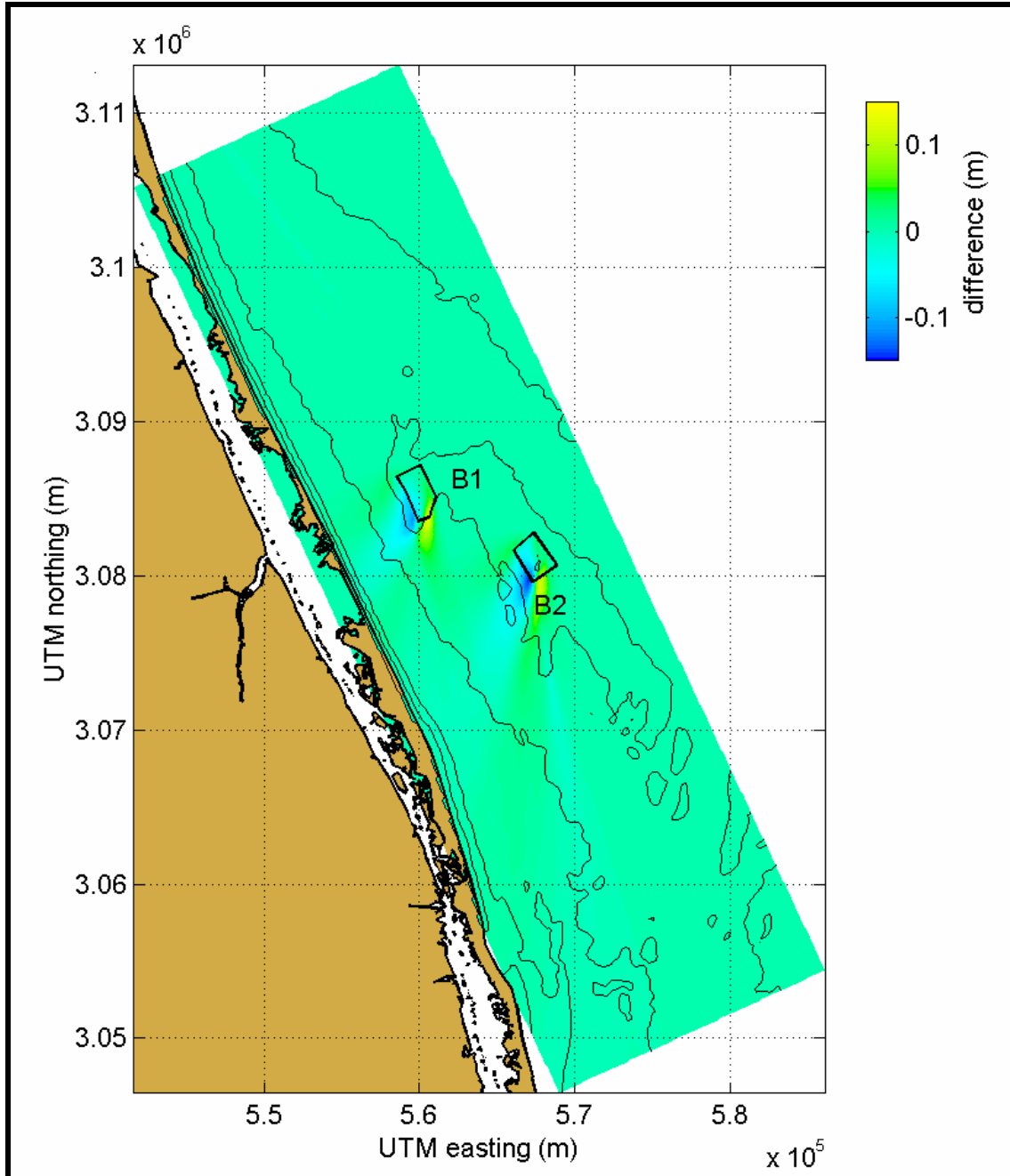


Figure 4-23. Wave height change between existing and post-dredging conditions at wave modeling Area B for STWAVE simulations, wave Case 1B ($H_s = 1.9$ m, $T_{peak} = 6.9$ sec, $\theta_{peak} = 25$ deg). Seafloor contours are shown at 5 m intervals. B1 is the borrow site in Sand Resource Area B1, and B2 is the borrow site in Sand Resource Area B2.

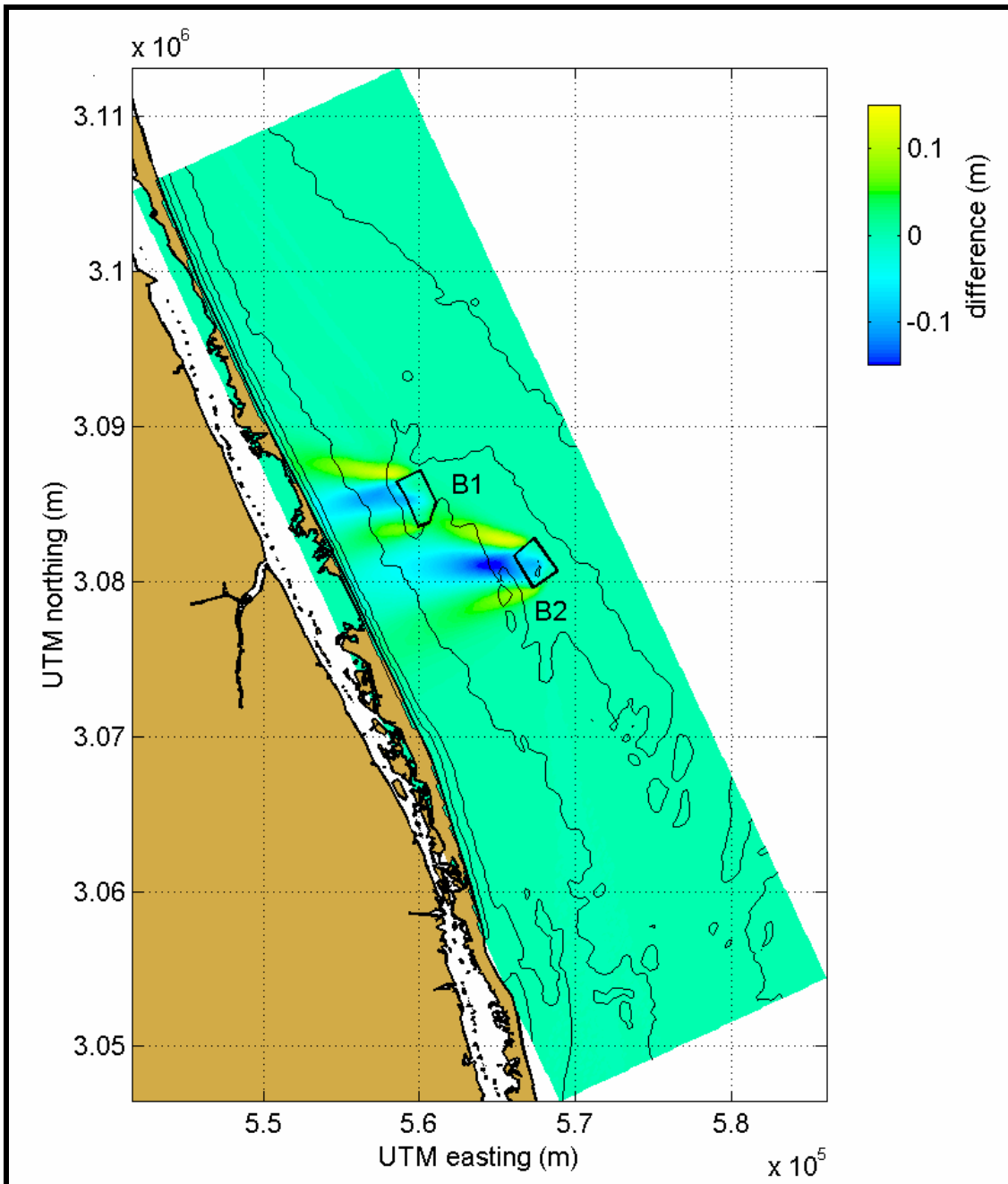


Figure 4-24. Wave height change between existing and post-dredging conditions at wave modeling Area B for STWAVE simulations, wave Case 10B ($H_s = 1.7$ m, $T_{peak} = 10.8$ sec, $\theta_{peak} = 90$ deg). Seafloor contours are shown at 5 m intervals. B1 is the borrow site in Sand Resource Area B1, and B2 is the borrow site in Sand Resource Area B2.

4.2.1.3 Area C

Examples of wave model output for Area C borrow sites are shown in Figures 4-25 through 4-28. Figure 4-25 shows coarse grid results for wave Case 2C, a 1.5 m, 7.5 sec wave from the NE. For this case, slight wave focusing was identified at shoals within the designated borrow site boundaries. The minimum depth at C1 north was 7.6 m NGVD, and 5.4 m NGVD was the minimum depth at Site C1 south. Because shallower depths existed in

these areas, waves passing over the shoals turned toward the shoreline sooner than in other areas the same distance offshore. Waves refracting over the shoals produced an area of increased wave heights landward of each shoal and a corresponding area of decreased wave heights immediately south of both sites. For the shoal within C1 north, maximum wave height increase was 0.18 m, and the maximum decrease was 0.39 m. Similar changes were observed at C1 south, where the maximum increase in wave height was 0.13 m and the maximum decrease was 0.33 m. Other features outside the two designated borrow sites affected waves in this region. A ridge centered at E 578400, N 3026200, approximately 3 km offshore, had a smaller impact on wave heights. Wave refraction over this shoal is potentially more significant than the impact to waves from shoals farther offshore because it is closer to shore and its area of influence is more focused along the shoreline.

For wave Case 10C, a 1.1 m, 11.1 second wave from the east (Figure 4-26), wave height changes at C1 north and C1 south were not as large as those for Case 2C, but wave energy was still focused behind the shoals. This focusing caused a zone of increased wave heights that extended to the shoreline. Unlike the results of Case 2C, where wave height changes at the borrow sites were more pronounced, the resulting wave shadow zone diffuses more as it approached the shoreline (due to the shorter peak wavelength of Case 2C).

The plot of wave height differences resulting from dredging Sites C1 north and C1 south are illustrated in Figure 4-27 for wave Case 2C. There seems to be a strong interaction between the two sites because C1 south is partially within the shadow zone of C1 north. The alignment of borrow sites caused a single area of increased wave heights at the shoreline (approximately 4 km long) and a more diffuse zone of reduced wave heights (extending 12 km toward St. Lucie Inlet). At the borrow sites, maximum wave height increase was 0.09 m, and the maximum wave height decrease was 0.15 m.

Wave height differences for wave Case 10C (Figure 4-28) illustrated that the borrow sites have an overlapping influence at the shoreline for waves propagating from the east, even though one site was not directly in the shadow of the other. The total length of affected shoreline was approximately 16 km. Wave height changes exhibited a typical impact pattern for two areas of increased wave heights flanked by a single area of reduced wave heights. Changes at the borrow sites were similar in magnitude to those for Case 2C. The resulting wave shadow zone for the two borrow sites was less diffuse due to a longer peak wavelength for this model case.

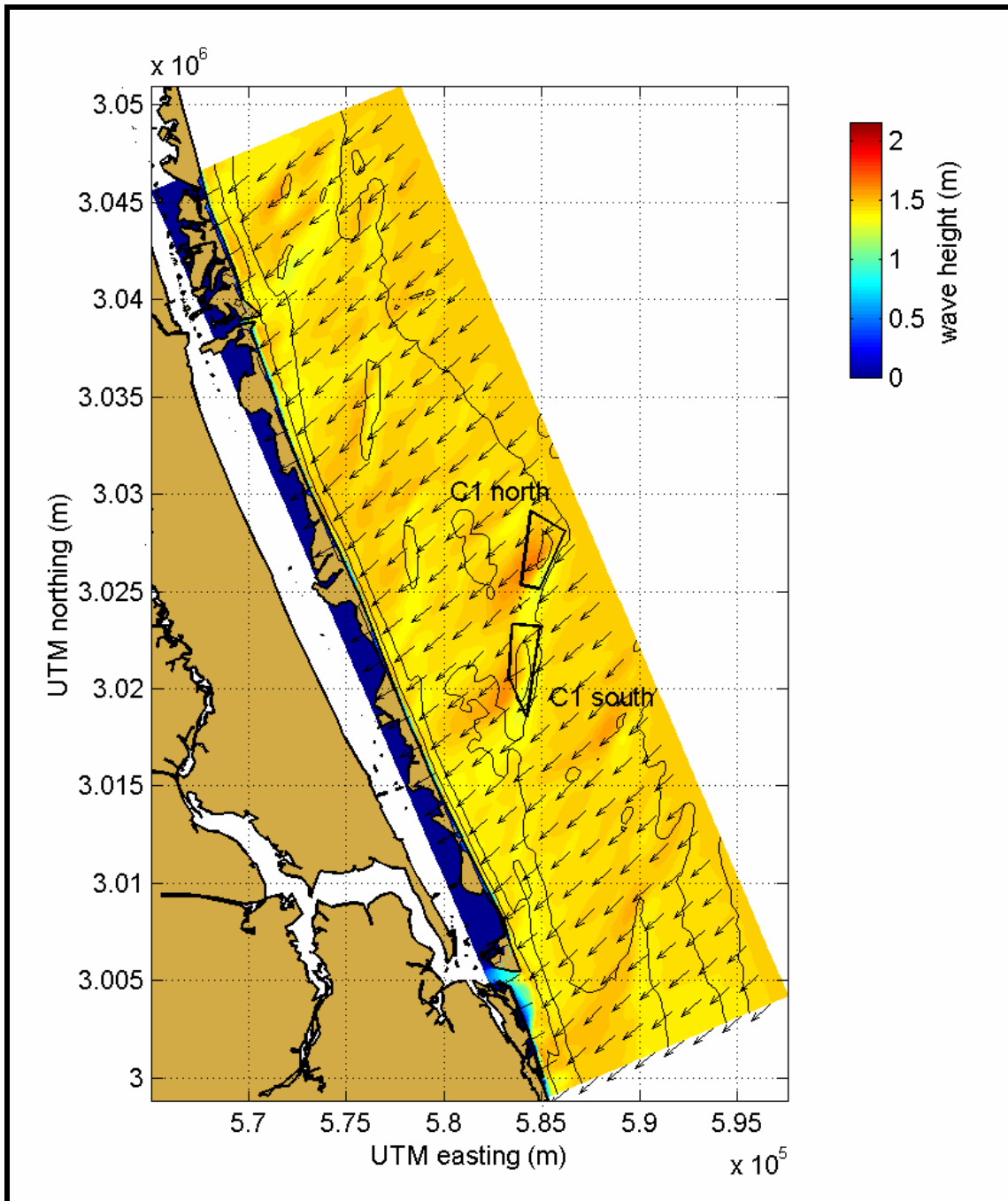


Figure 4-25. STWAVE output for wave modeling Area C, wave Case 2C ($H_s = 1.5$ m, $T_{peak} = 7.5$ sec, $\theta_{peak} = 47$ deg). Color contours indicate wave height, and vectors show mean direction of wave propagation. Seafloor contours are shown at 5 m intervals. C1 north and C1 south are the northern and southern borrow sites in Sand Resource Area C1.

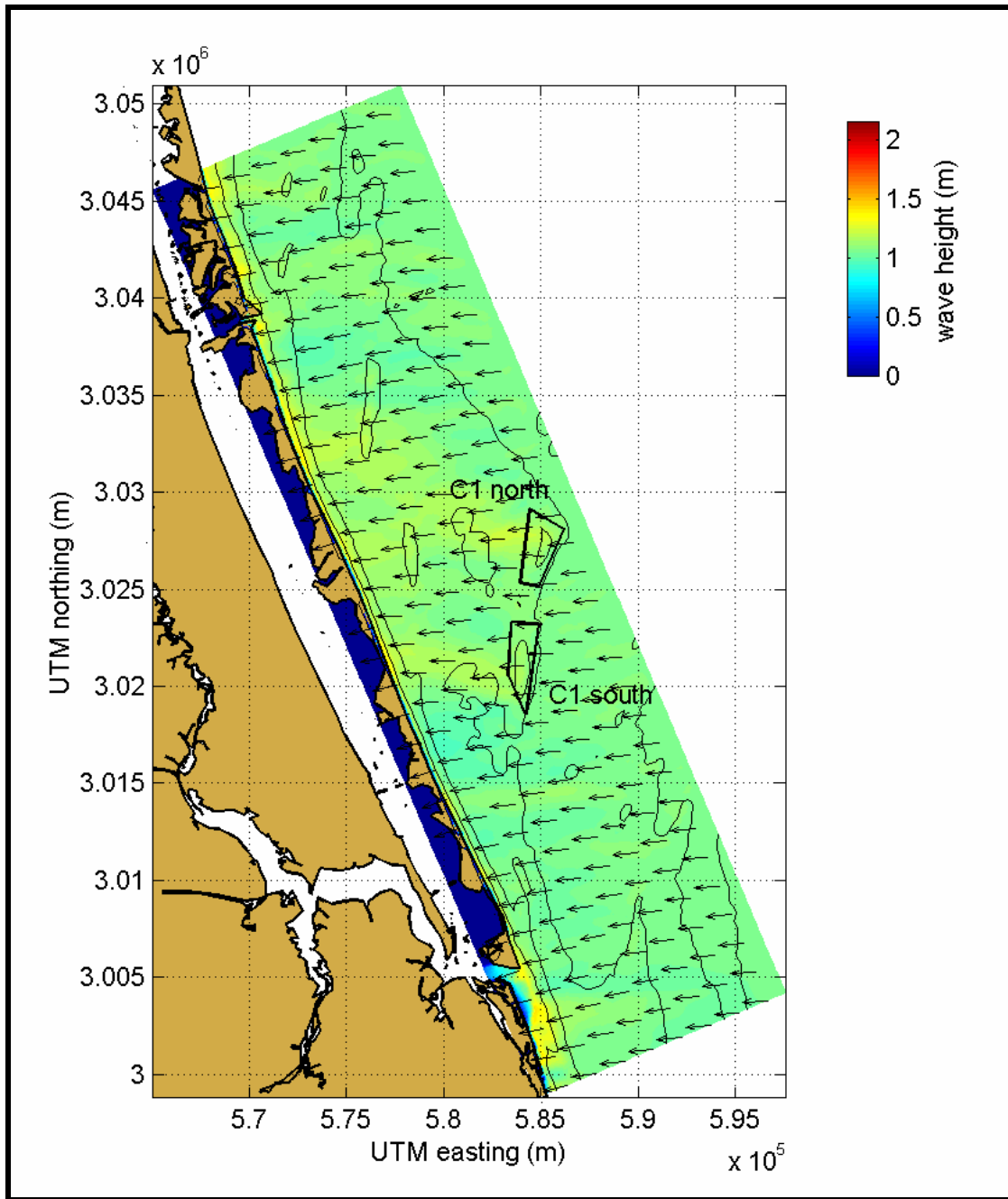


Figure 4-26. STWAVE output for wave modeling Area C, wave Case 10C ($H_s = 1.1$ m, $T_{peak} = 11.1$ sec, $\theta_{peak} = 87$ deg). Color contours indicate wave height, and vectors show mean direction of wave propagation. Seafloor contours are shown at 5 m intervals. C1 north and C1 south are the northern and southern borrow sites in Sand Resource Area C1.

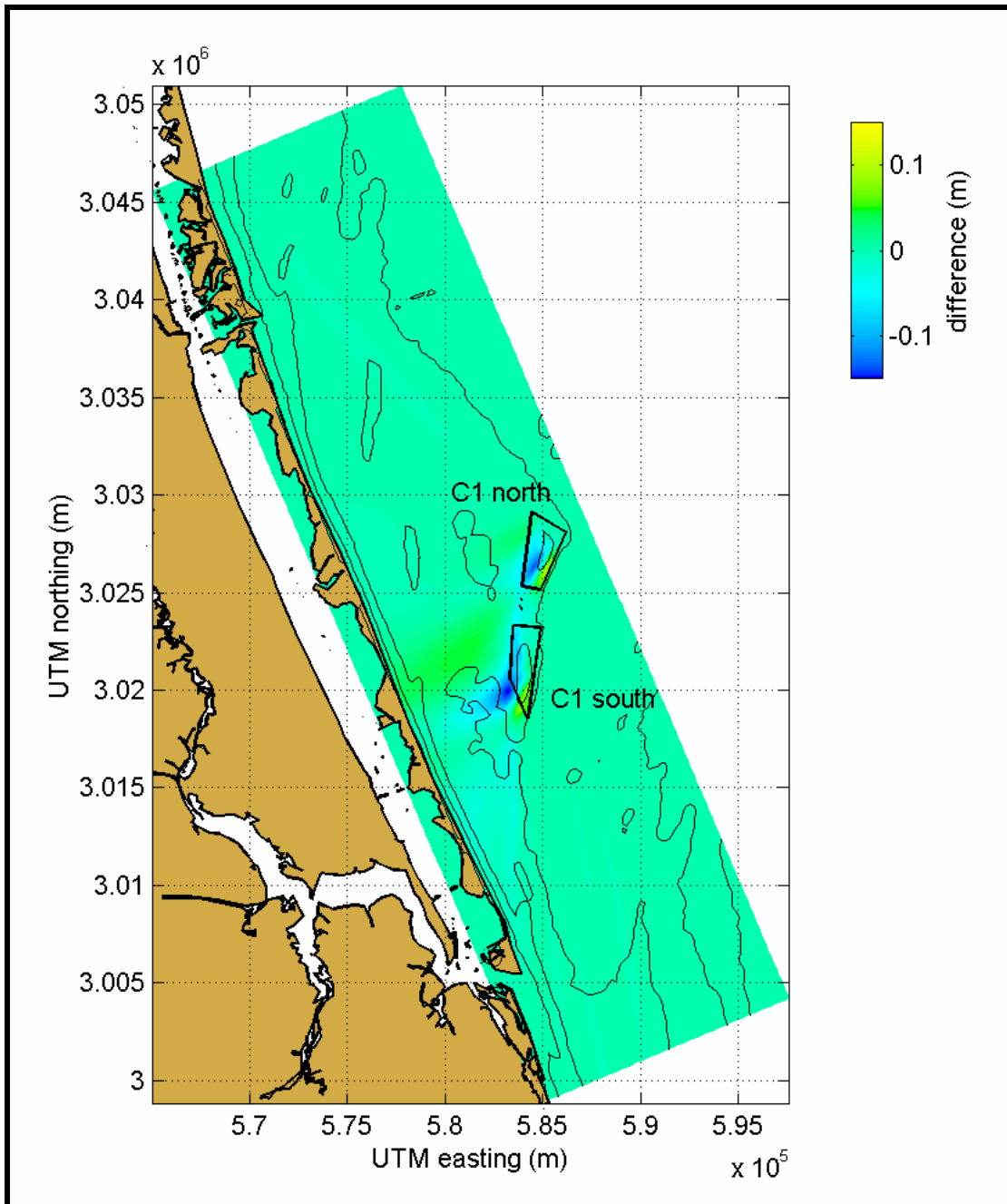


Figure 4-27. Wave height change between existing and post-dredging conditions at wave modeling Area C for STWAVE simulations, wave Case 2C ($H_s = 1.5$ m, $T_{peak} = 7.5$ sec, $\theta_{peak} = 47$ deg). Seafloor contours are shown at 5 m intervals. C1 north and C1 south are the northern and southern borrow sites in Sand Resource Area C1.

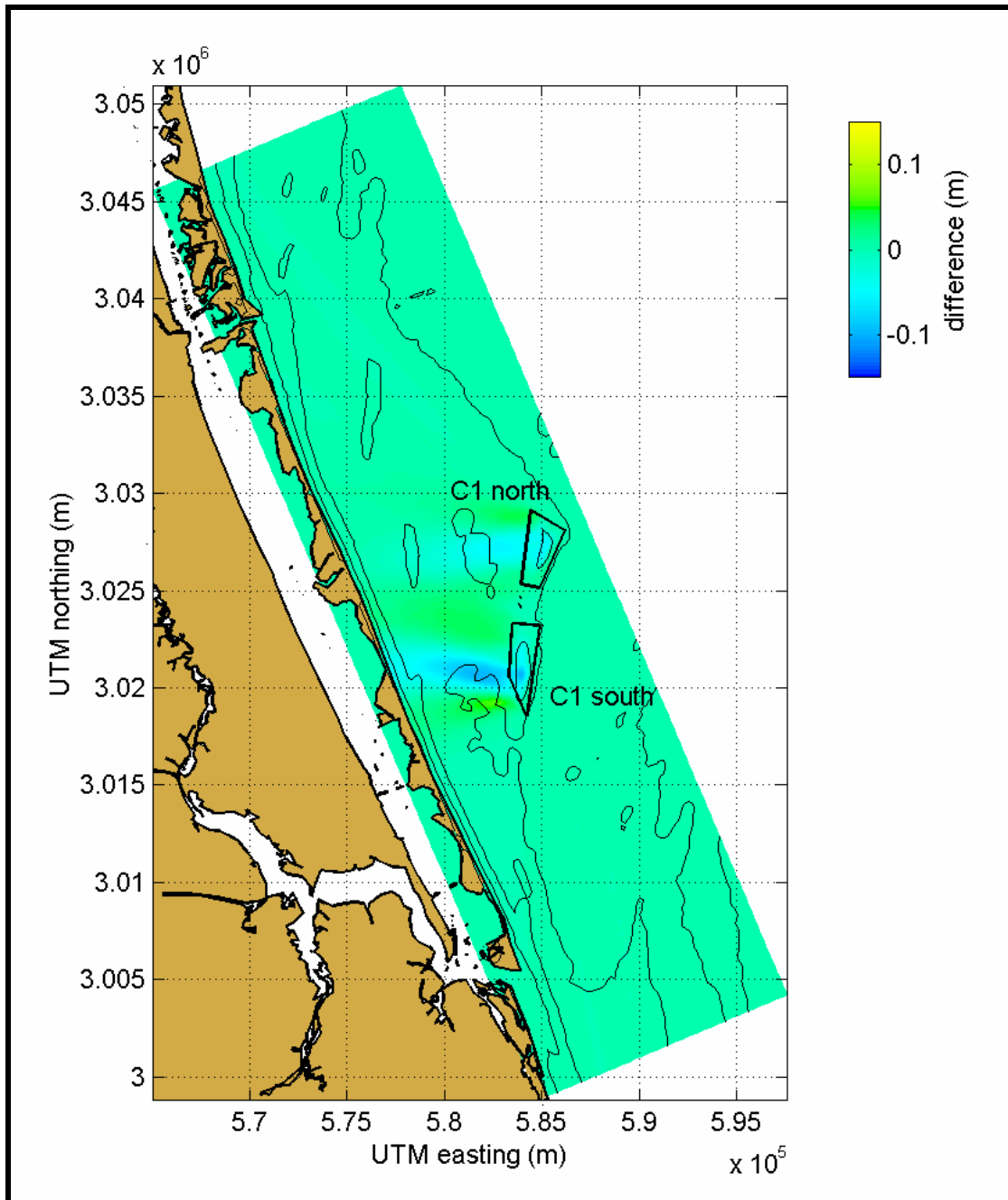


Figure 4-28. Wave height change between existing and post-dredging conditions at wave modeling Area C for STWAVE simulations, wave Case 10C ($H_s = 1.1$ m, $T_{peak} = 11.1$ sec, $\theta_{peak} = 87$ deg). Seafloor contours are shown at 5 m intervals. C1 north and C1 south are the northern and southern borrow sites in Sand Resource Area C1.

4.2.1.4 Area D

Wave model output for Area D (Jupiter Inlet) is shown in Figures 4-29 through 4-32. Results from wave Case 1D, a 1.4 m, 6.9 sec wave from the NNE, are shown in Figure 4-29. The primary bathymetric feature in this region is a shoal area centered at E 595200, N 2987800, approximately 5.6 km offshore Jupiter Inlet. The shoal has a minimum water depth of 11.7 m NGVD. The borrow site designed for this area (D2) lies along the seaward

margin of the shoal at the Federal-State boundary in relatively deep water. For wave Case 1D, the shoal influenced wave refraction patterns, resulting in a slight focusing of waves seaward of the shoal and an area of reduced wave heights 2.6 km along the shoreline north of Jupiter Inlet. Similar results were documented for wave Case 9D, a 1.3 m, 13.0 sec wave from the east-northeast (Figure 4-30). Wave heights increased behind the shoal, and a 4.9 km stretch of coastline north of Jupiter Inlet experienced increased wave heights. Maximum wave height increase caused by the shoal for Case 9D was 0.4 m, whereas Case 1D produced a 0.1 m change in wave height.

Wave height changes resulting from dredging Borrow Site D2 are documented in Figure 4-31. For wave Case 1D, the greatest change occurred at the north end of the site where the deepest excavation occurred. The maximum increase and decrease in wave height that resulted for this wave condition was 0.04 and 0.05 m, respectively. This small change relative to changes at borrow sites to the north was due to greater water depths at and seaward of Borrow Site D2.

For wave Case 9D, two shadow areas of reduced wave heights propagated from two separate areas within the borrow site, but join to form one shadow on the shoreward side of the shoal (Figure 4-32). This change pattern occurred because the original bathymetry within Site D2 contained two elevation peaks approximately 1.5 m higher than the surrounding shoal surface.

4.2.2 Sediment Transport Potential

Comparisons of average annual sediment transport potential were performed for existing and post-dredging conditions to document the relative impact of dredging at borrow sites on longshore sediment transport processes. Sediment transport potential is a useful indicator of shoreline impacts caused by offshore borrow sites because the computations include the borrow site influence on wave height and direction. Although largest changes to the wave field occur at a borrow site, impacts cannot be adequately assessed without determining the resulting impact to coastal processes at the shoreline. As an example, a large borrow site that causes a large change in wave height at the site, but is far offshore, could have less shoreline impact than a much smaller site located closer to shore.

The net sediment transport potential associated with average annual conditions (Tables 4-1 through 4-4) was computed for shorelines landward of proposed sand borrow sites. Transport potential was computed using fine grid model results. In addition to average annual results, wave model simulations and sediment transport potential calculations were performed for 20 individual years of WIS data to provide information necessary to develop a $\pm 0.5\sigma$ transport significance envelope. Wave modeling for 20 individual years proceeded in a similar fashion to the modeling effort for average annual conditions (i.e., wave data for each separate year was binned according to direction and period to develop several wave cases for each year). Results for Area A1 were based on an earlier form of the transport significance criterion. Application of this method used $\pm 1\sigma$ as the significance criterion based on splitting the 20-year wave-hindcast record into five 4-year periods as opposed to 20 individual. For this study, more than 1,000 individual wave model runs were completed to determine average annual conditions and associated transport significance envelopes.

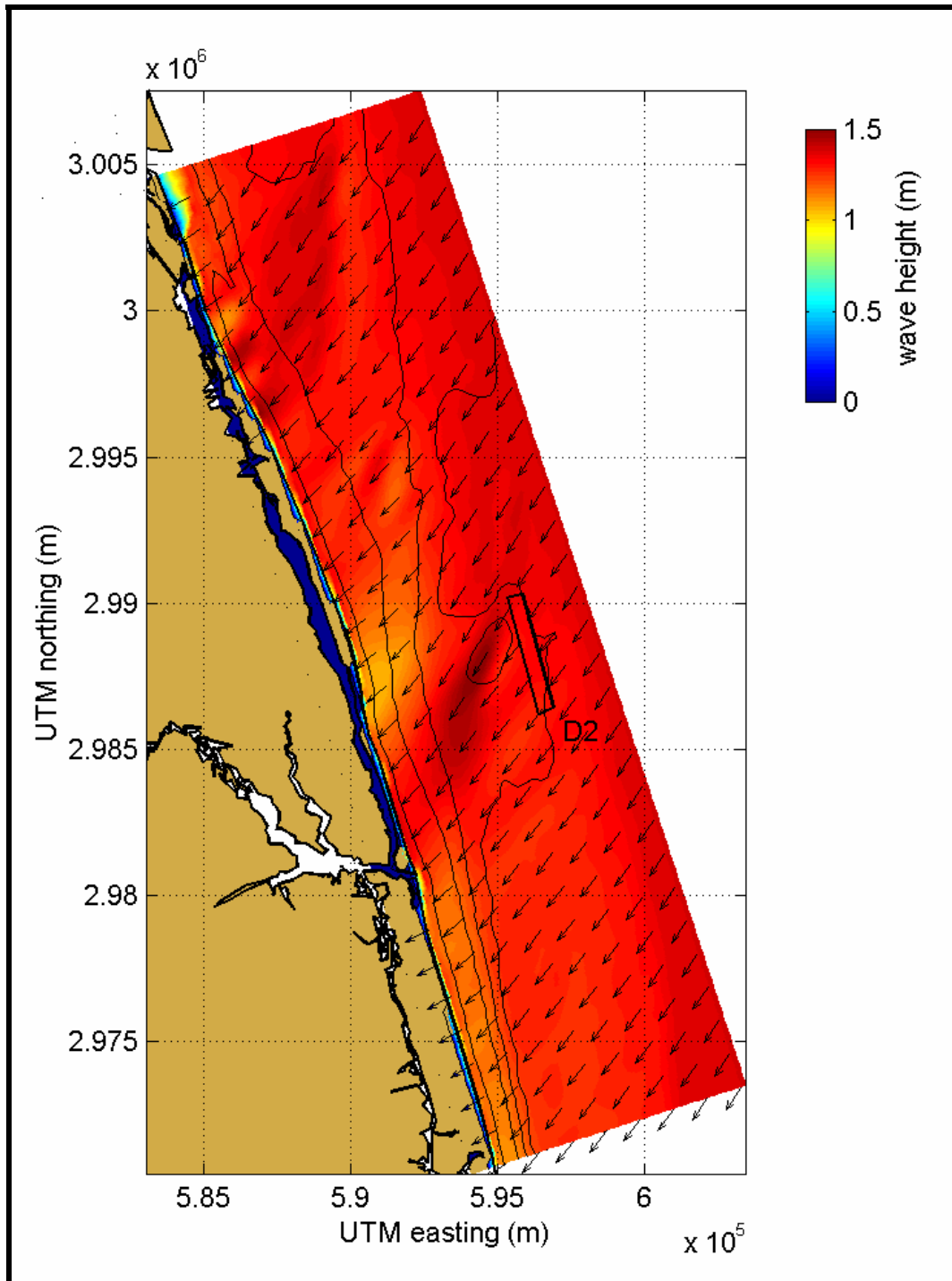


Figure 4-29. STWAVE output for wave modeling Area D, wave Case 1D ($H_s = 1.4$ m, $T_{peak} = 6.9$ sec, $\theta_{peak} = 32$ deg). Color contours indicate wave height, and vectors show mean direction of wave propagation. Seafloor contours are shown at 5 m intervals. D2 is the borrow site that extends from Sand Resource Area D1 into Sand Resource Area D2 along the Federal-State boundary.

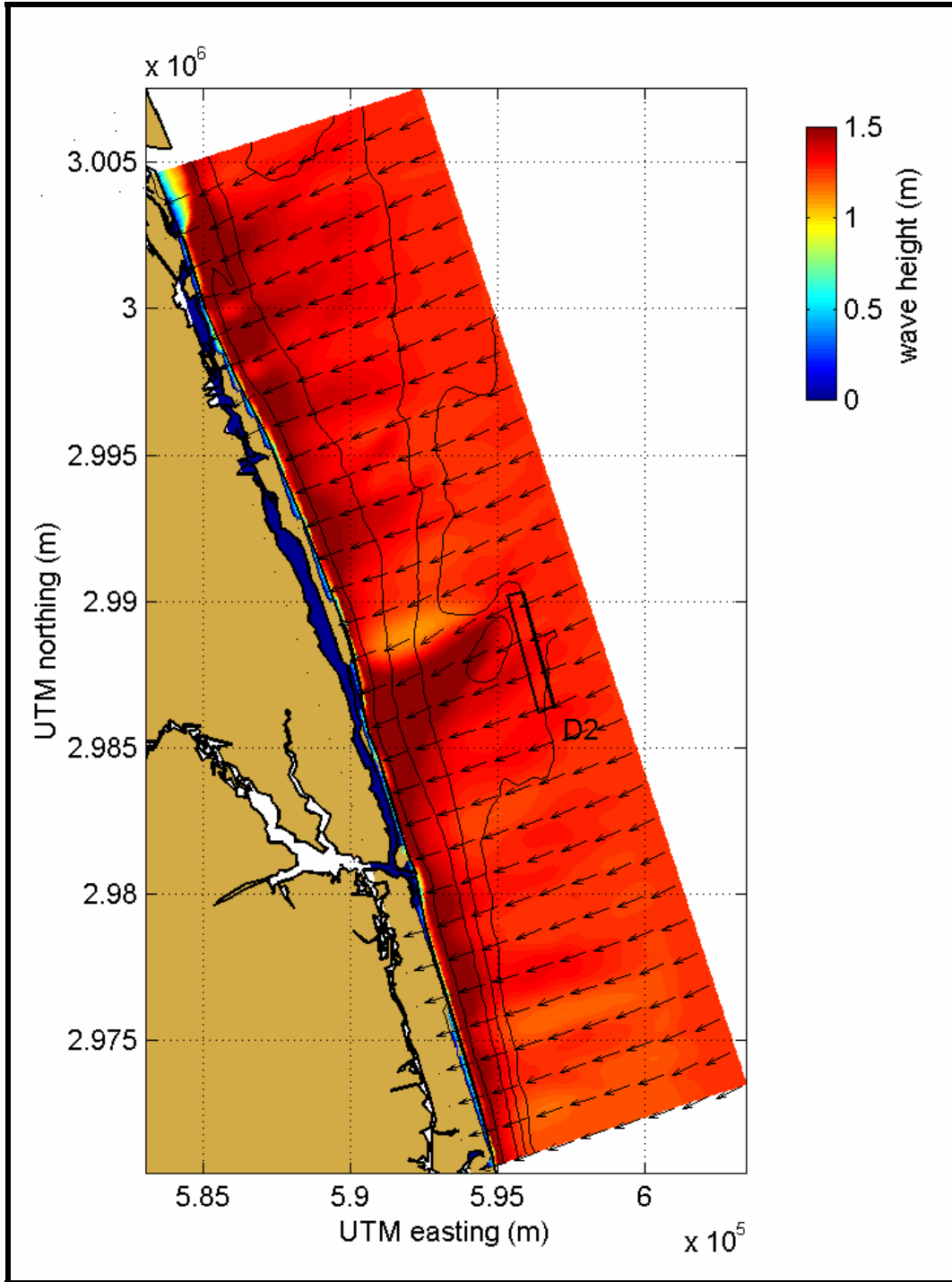


Figure 4-30. STWAVE output for wave modeling Area D, wave Case 9D ($H_s = 1.3$ m, $T_{peak} = 13.0$ sec, $\theta_{peak} = 62$ deg). Color contours indicate wave height, and vectors show mean direction of wave propagation. Seafloor contours are shown at 5 m intervals. D2 is the borrow site that extends from Sand Resource Area D1 into Sand Resource Area D2 along the Federal-State boundary.

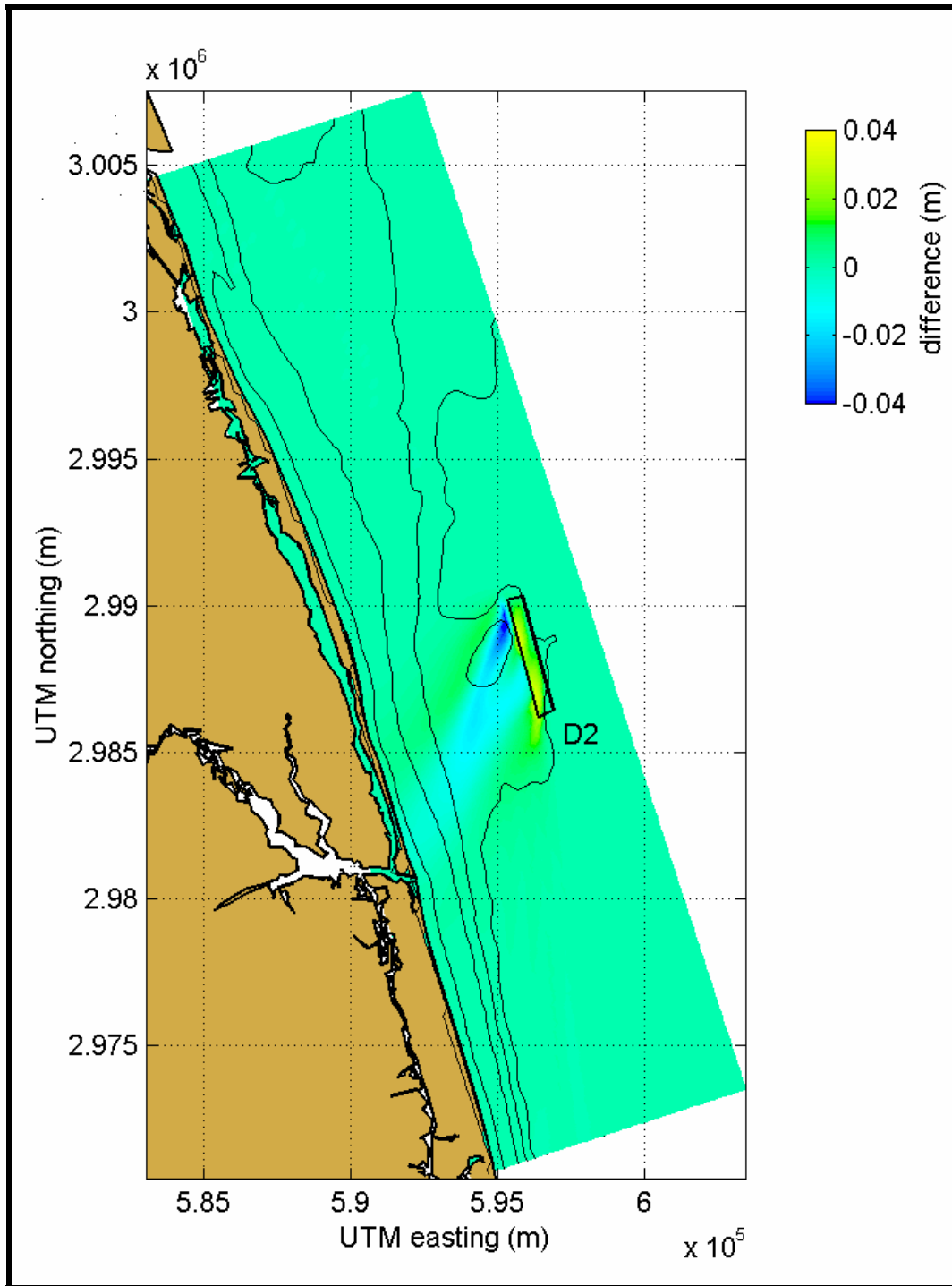


Figure 4-31. Wave height change between existing and post-dredging conditions at wave modeling Area D for STWAVE simulations, wave Case 1D ($H_s = 1.4$ m, $T_{peak} = 6.9$ sec, $\theta_{peak} = 32$ deg). Seafloor contours are shown at 5 m intervals. D2 is the borrow site that extends from Sand Resource Area D1 into Sand Resource Area D2 along the Federal-State boundary.

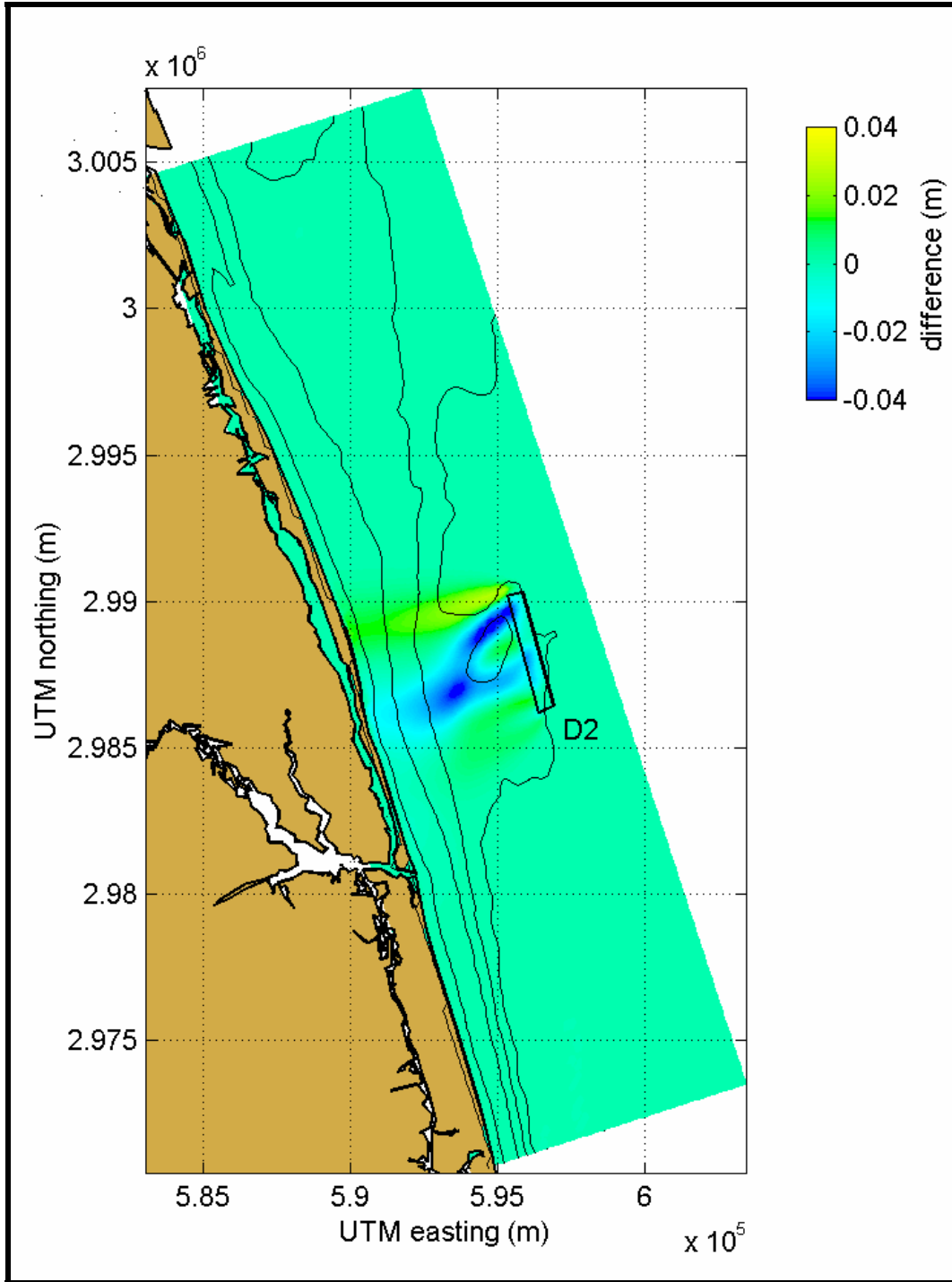


Figure 4-32. Wave height change between existing and post-dredging conditions at wave modeling Area D for STWAVE simulations, wave Case 9D ($H_s = 1.3$ m, $T_{peak} = 13.0$ sec, $\theta_{peak} = 62$ deg). Seafloor contours are shown at 5 m intervals. D2 is the borrow site that extends from Sand Resource Area D1 into Sand Resource Area D2 along the Federal-State boundary.

Mean sediment transport potential calculated for Area A (adjacent to Cape Canaveral) for the modeled 20-year period is illustrated with computed transport curves of the 20 individual years used in the determination of the $\pm\sigma$ significance envelope (Figure 4-33). The shoreline south of Port Canaveral indicated strong net southerly transport of approximately 500,000 m³/yr, which gradually reduced to approximately 300,000 m³/yr at the southern limit of the model grid. The significance envelope was largest (approximately $\pm 300,000$ m³/yr) north of Cape Canaveral and in the southern half of the modeled area, and it reduced to approximately $\pm 50,000$ m³/yr just north of Port Canaveral. The relatively small significance envelope for this section of shoreline suggested that inter-annual variability of mean sediment transport was small due to the sheltering effect of Cape Canaveral and Canaveral Shoals.

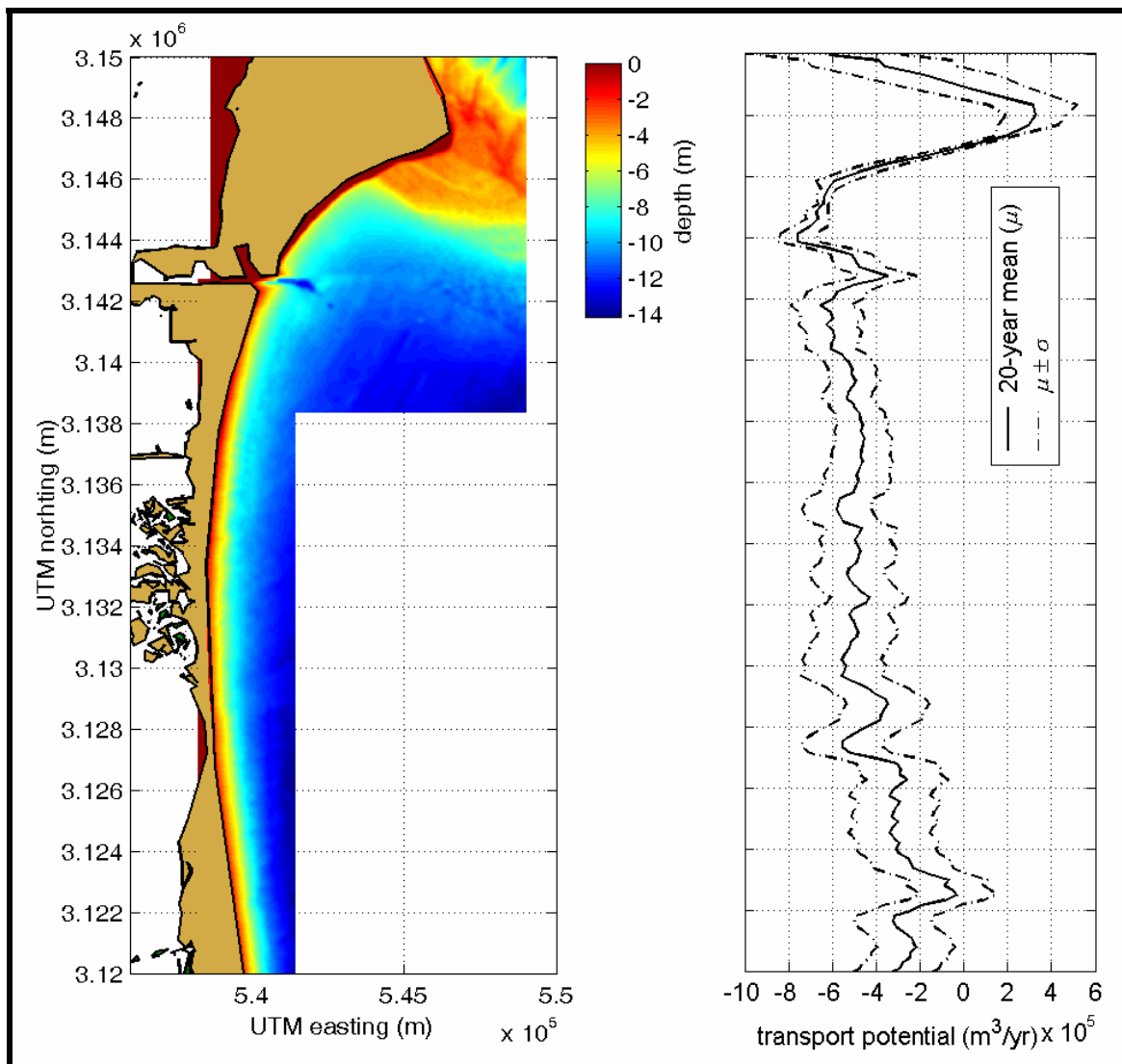


Figure 4-33. Average annual sediment transport potential (solid black line) computed for the shoreline landward of the borrow site in Area A1 (Port Canaveral). Positive transport potential is directed to the north and negative transport potential is directed to the south. The black dot-dash lines indicate the $\pm\sigma$ significance envelope about the mean net transport rate.

Average annual results for modeled Area A documented gross northerly- and southerly-directed transport potential (Figure 4-34), with average net transport, for the 20-year modeled period. The modeled shoreline generally had a strong south-oriented transport potential between the cusp of Cape Canaveral and Port Canaveral. Between Port Canaveral and the southern limit of the grid, potential transport gradually became less southerly dominated, with gross northerly transport rates (~200,000 m³/yr) that were roughly half of gross southerly transport rates.

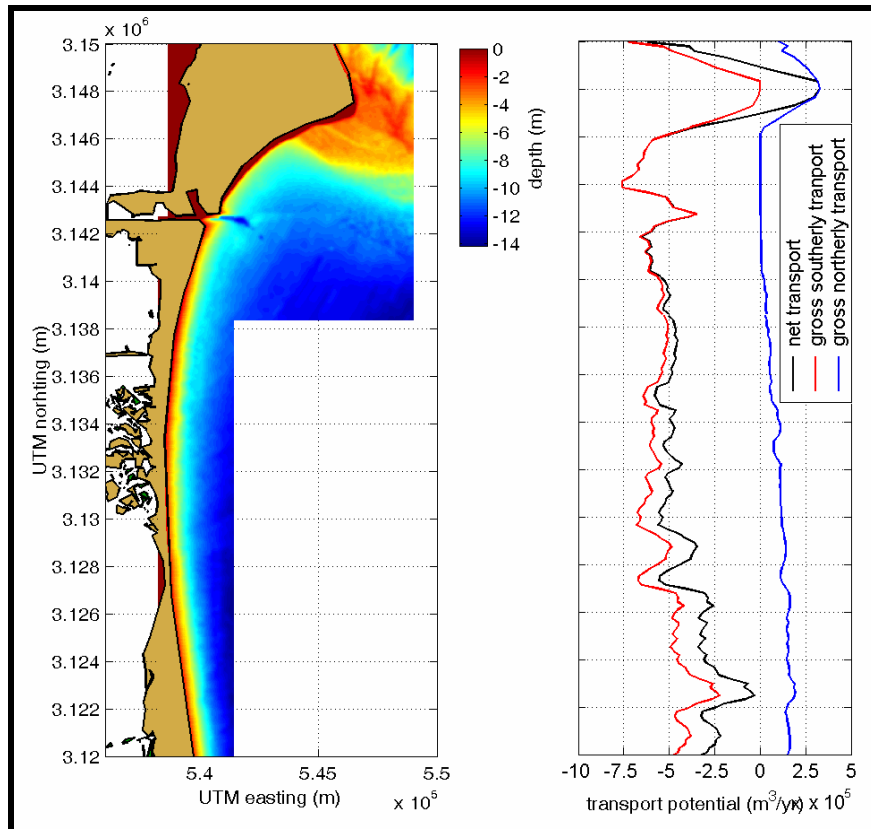


Figure 4-34. Average net transport potential (black line) with gross southerly- and northerly-directed transport potential (red and blue lines, respectively) for the shoreline landward of Area A1.

Mean transport potential computed for Area B for the modeled 20-year period is shown with computed transport curves for the 20 individual years used to determine the $\pm 0.5\sigma$ significance envelope (Figure 4-35). Results indicated that along the coastline from N 3,090,000 to N 3,065,000, net transport potential was generally less than 100,000 m³/yr to the south. There was an approximate $\pm 500,000$ m³/yr range in annual net transport rates. Along this shoreline, results indicated that it was possible in some years for net transport potential to be northward directed. South of N 3,065,000, net transport potential was to the south at around 500,000 m³/yr. This may be due to a change in shoreline orientation that occurred at this point. The annual variation in net transport potential was similar (approximately $\pm 500,000$ m³/yr) for the shoreline north of the break. For the length of modeled shoreline, the year with greatest modeled southerly transport was 1980, and the year with greatest northerly transport was 1990.

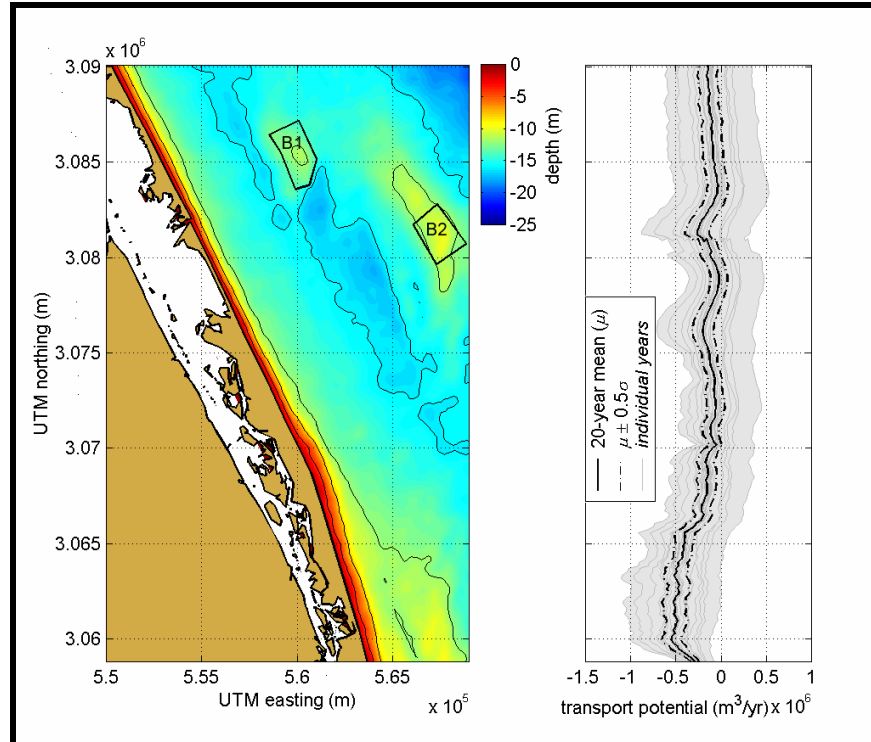


Figure 4-35. Average annual sediment transport potential (solid black line) computed along the shoreline landward of borrow sites in Areas B1 and B2 (Sebastian Inlet). Positive transport potential is directed to the north and negative transport potential is directed to the south. Net transport potential curves determined for 20 individual years of WIS data are indicated by the gray shaded area. The $\pm 0.5\sigma$ significance envelope (black dot-dash lines) about the mean net transport rate was determined using the 20 net potential curves. B1 is the borrow site in Sand Resource Area B1, and B2 is the borrow site in Sand Resource Area B2.

Average annual results for modeled Area B show the breakdown of gross northerly- and southerly-directed transport potential (Figure 4-36), with average net transport, for the 20-year modeled period. The modeled shoreline generally had bi-directional transport of approximately $400,000 \text{ m}^3/\text{yr}$, which resulted in a much smaller net potential, directed to the south. South of N 3,065,000, north-directed transport decreased and south-directed transport increased. The result was an increase in net transport to the south.

Computed mean annual transport potential for modeled Area C was to the south, ranging from approximately $400,000 \text{ m}^3/\text{yr}$ at the northern boundary of the study area to approximately $100,000 \text{ m}^3/\text{yr}$ at the southern limit near St. Lucie Inlet (Figure 4-37). Sand transport potential calculations for 20 individual years indicated that the annual variability in transport potential had a range of approximately $\pm 400,000 \text{ m}^3/\text{yr}$ to the north that gradually decreases to approximately $\pm 200,000 \text{ m}^3/\text{yr}$ at the southern limit of the modeled area. Along some sections of the modeled shoreline, it was possible to have net northerly-directed transport during some of the years. Similar to the results for Area B, the year with greatest modeled southerly transport was 1980, and the year with greatest northerly transport was 1990. For the mean transport curve, there was a local minimum that occurred at N 3026500. This likely resulted from the presence of the shoal ridge centered at E 578400 N 3026200, approximately 3 km offshore.

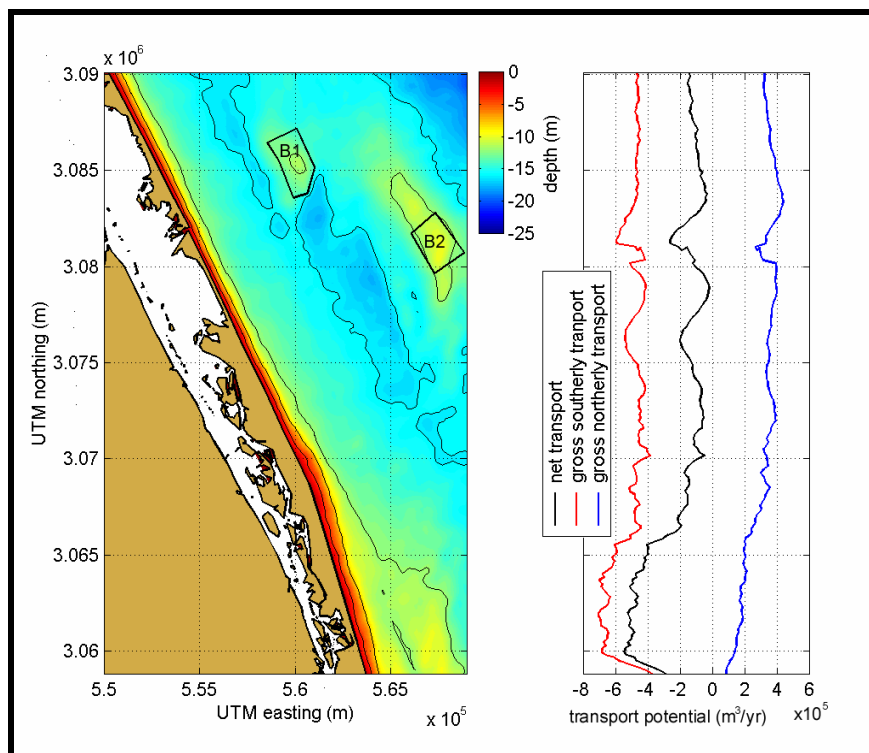


Figure 4-36. Annual net transport potential (black line) with gross southerly- and northerly-directed transport (red and blue lines, respectively) for the shoreline landward of B1 and B2. B1 is the borrow site in Sand Resource Area B1, and B2 is the borrow site in Sand Resource Area B2.

Average annual results for modeled Area C showed the breakdown of gross northerly- and southerly-directed transport potential (Figure 4-38), with the average net transport, for the 20-year modeled period. The transport potential along this shoreline was more strongly to the south than for Area B. Toward St. Lucie Inlet, transport potential becomes more bi-directional, as there was a decrease in gross southerly transport and an increase in gross northerly transport potential.

Net transport along the coastline landward of Area D (Jupiter Inlet) varied from about 200,000 m³/yr to the south near the northern limit of the area to about 500,000 m³/yr to the south near Jupiter Inlet (Figure 4-39). Results from the 20 individual modeled years showed that the annual variability ranged from approximately $\pm 150,000$ m³/yr in the northern part of Area D to approximately $\pm 300,000$ m³/yr at the southern extent of the model grid. At its greatest, net transport potential varied by about $\pm 500,000$ m³/yr near N 2985000 (gray shaded area on Figure 4-39). Similar to modeled Areas B and C, the year with greatest modeled southerly transport was 1980, and the year with greatest northerly transport was 1990. As with the entire study area, net transport potential was always to the south. The large acceleration in south-directed transport between N 2,988,000 and N 2,986,000 indicated that the area between these locations was highly erosional. Historical data indicate that an erosional hot spot existed in this area (see Ramsey et al., 1995). Severe beach erosion has been a problem in the area called the "S" curve (N 2,987,600) where a north-south coastal roadway was diverted landward due to pervasive erosion.

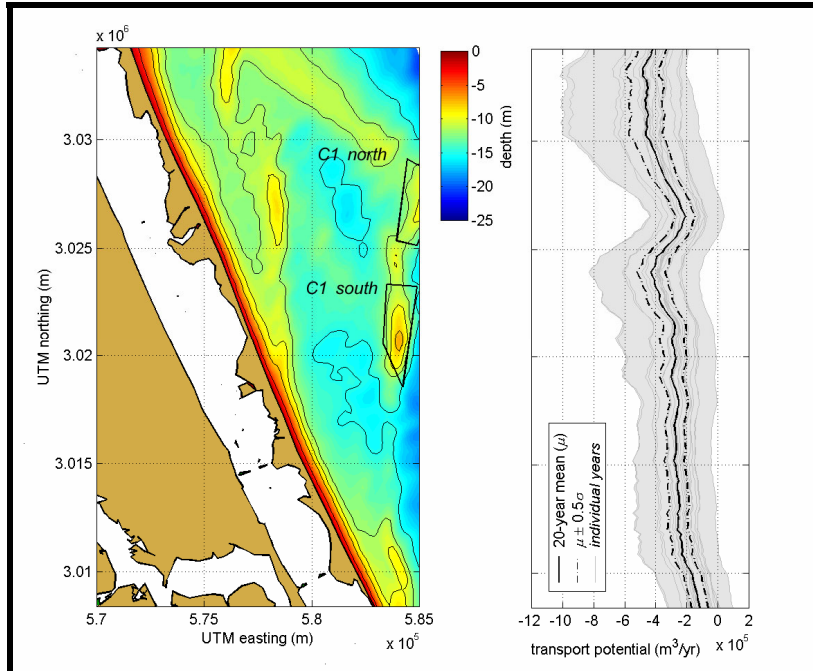


Figure 4-37. Average annual sediment transport potential (solid black line) computed along the shoreline landward of Borrow Sites C1 north and C1 south. Positive transport potential is directed to the north and negative transport potential is directed to the south. Net transport potential curves determined for 20 individual years of WIS data are indicated by the gray shaded area. The $\pm 0.5\sigma$ significance envelope (black dot-dash lines) about the mean net transport rate was determined using the 20 net potential curves. C1 north and C1 south are the borrow sites in Sand Resource Area C1.

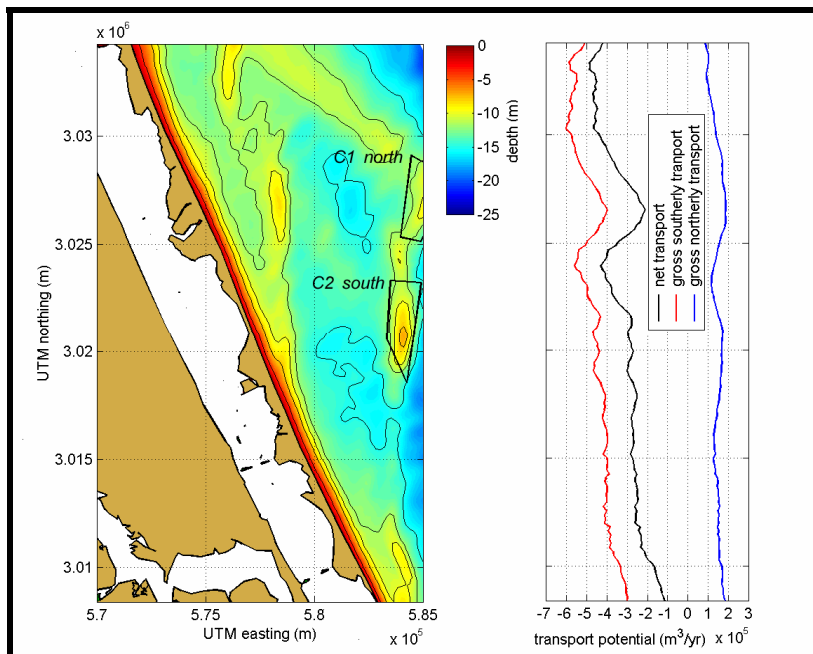


Figure 4-38. Annual net transport potential (black line) with gross southerly- and northerly-directed transport (red and blue lines, respectively) for the shoreline landward of C1 north and C1 south. C1 north and C1 south are the borrow sites in Sand Resource Area C1.

Results illustrated in Figure 4-40 document that the transport potential was strongly to the south. North of the “S” curve, gross northerly transport potential was approximately 100,000 m³/yr. South of this area, north-directed transport was almost zero, resulting in unidirectional transport to the south.

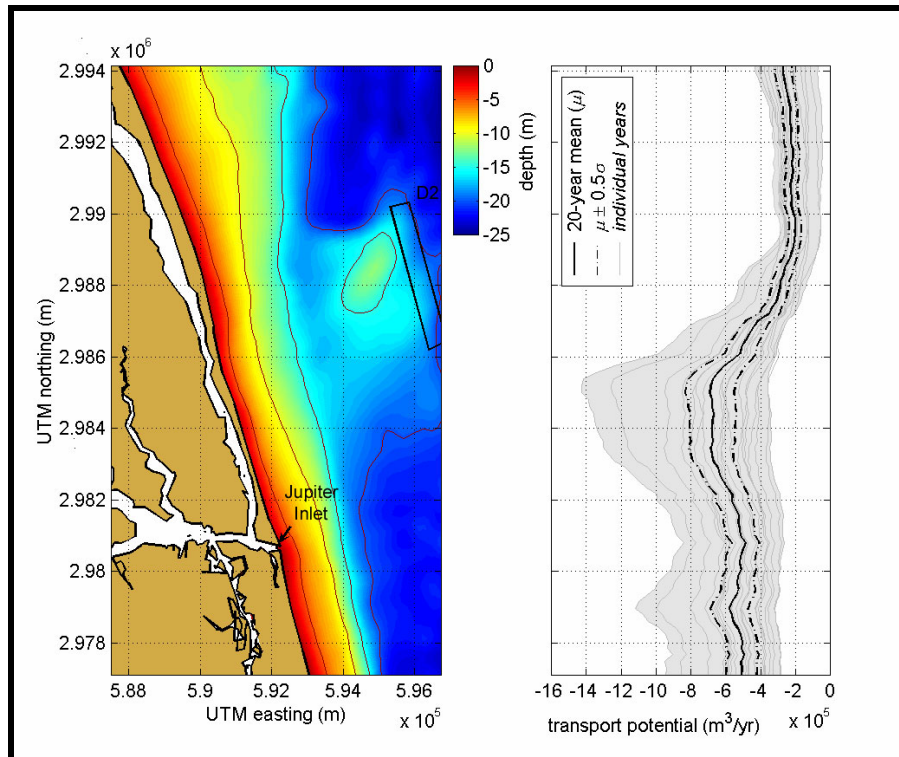


Figure 4-39. Average annual sediment transport potential (solid black line) computed along the shoreline landward of Borrow Site D2. Positive transport potential is directed to the north and negative transport potential is directed to the south. Net transport potential curves determined for 20 individual years of WIS data are indicated by the gray shaded area. The $\pm 0.5\sigma$ significance envelope (black dot-dash lines) about the mean net transport rate was determined using the 20 net potential curves. D2 is the borrow site in between Sand Resource Areas D1 and D2.

4.2.2.1 Model Comparison with Historical Shoreline Change

To ensure that spectral wave modeling and associated longshore sediment transport potential could be used effectively to evaluate long-term alterations to the littoral system, a comparison of model predictions with observed shoreline change was performed. This analysis provided a semi-quantitative method for determining whether a) wave-induced longshore transport was responsible for observed shoreline change, and b) long-term shoreline change trends were consistent with shorter time-period (20-year) sediment transport potential analyses. An evaluation of model output was performed using a comparison of computed gradients in sediment transport to historical shoreline change data. The basis for this comparison is the relationship between shoreline movement and the longshore gradient in sediment transport. Simply expressed, this relationship is

$$\frac{\partial Q}{\partial y} \propto \frac{\partial x}{\partial t} \tag{4.10}$$

where Q is sediment transport, y is alongshore distance, x is cross-shore position of the shoreline, and t is time. A comparison of results should illustrate similar trends in long-term shoreline change and transport potential computed using wave conditions that represent long-term average conditions. The gradient in sediment transport potential was not expected to perfectly simulate this process, but good general agreement between these two quantities would suggest that the transport potential model reasonably represented long-term coastal processes for a given area, and thus, the model's ability to predict likely impacts that may result from offshore dredging.

The time variation in shoreline position was determined from an analysis of historical shoreline data for each of the study areas. Regional change analysis provided a without-project assessment of shoreline response for comparison with predicted changes in wave-energy focused at the shoreline resulting from potential offshore sand dredging activities. Because continuous measurements of historical shoreline change are available at 50-m alongshore intervals (see Section 3.0), model results (wave and sediment transport) at discrete intervals along the coast can be compared with historical data to develop process/response relationships for evaluating potential impacts.

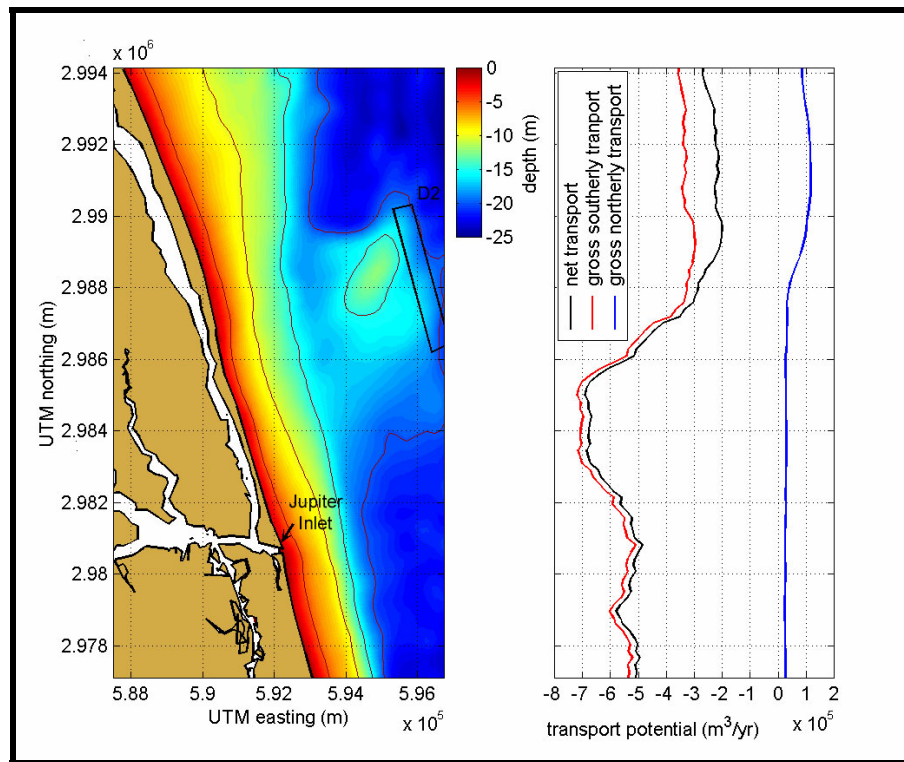


Figure 4-40. Annual net transport potential (black line) with gross southerly- and northerly-directed transport (red and blue lines, respectively) for the shoreline landward of the borrow site in modeled Area D. D2 is the borrow site between Sand Resource Areas D1 and D2.

Model results and shoreline change data for modeled Area A, seaward of Cape Canaveral, are illustrated in Figure 4-41 (Kelley et al., 2001). Analyses indicate that the shoreline was stable about 6 km south of Port Canaveral. Shoreline change results showed net accretion from the Cape south to Port Canaveral for all time periods (see Section 3.0).

This trend was not replicated for modeled transport gradients, which showed an area of high accretion at the Cape followed by an area of significant erosion between the Cape and Port Canaveral. The model had difficulty predicting transport rates in this area due to complex offshore bathymetric features associated with Canaveral Shoals and limitations related to wave modeling under diffracting conditions. Furthermore, STWAVE propagates wave energy within a ± 90 degree sector from the cross-shore axis of the grid, which is important in areas where the shoreline angle is steep relative to the axis of the grid (e.g., just south of Cape Canaveral).

Based on shoreline curvature north of Port Canaveral, significant erosion was predicted immediately south of the cusp of Cape Canaveral (as indicated by the modeled gradient of transport potential). However, historical shoreline change data indicated substantial accretion in this area. The primary reason for this accretion likely was due to the shoal serving as a sediment source for beaches to the south. This cross-shore transport mechanism was not considered in longshore sediment transport predictions. For shorelines where nearshore shoals exhibit significant diffraction and potentially serve as a sediment source to the beach system, modeled sediment transport potential may not match observed trends in shoreline change. South of Port Canaveral, away from the influence of Cape topographic and bathymetric features, trends predicted by the sediment transport potential model match well with historical shoreline change.

For Area B, long-term shoreline change data covering the periods 1877 to 1970 were used to quantify trends (see Section 3.0). An additional analysis of short-term (1972 to 1993) shoreline change trends was completed using beach profile data available from the FDEP. Short-term analysis was performed to provide an estimate of shoreline change for a period of time similar to that covered by the WIS wave dataset. Methods used for compiling and analyzing historical data sets are described in Section 3.0. Alongshore variations in sand transport were determined using computed values of transport potential for modeled existing conditions for each shoreline.

Modeled sand transport gradients for Area B generally agreed with trends in shoreline change (Figure 4-42). Long-term (1877 to 1970) shoreline change rates illustrated that this area was generally stable, with less than 0.5 m/yr changes in shoreline position in most areas. Change rates were greatest in the vicinity of Sebastian Inlet (N 3081900). Short-term (1972 to 1993) shoreline change rates exhibited greater variability, but the trend documented a fairly stable to slightly erosional shoreline. The computed gradient in sediment transport potential indicated fairly stable conditions, with no major accretional or erosional hot spots. Minor differences between the two results exist near Sebastian Inlet. However, the computational method for determining gradients in transport was not expected to calibrate well in areas where jetties or groins exist. Overall, good agreement existed between observed shoreline change and longshore gradient in modeled transport potential.

For modeled Area C, long-term and short-term shoreline change rates indicated that the modeled area was stable to erosional, with change rates generally less than 0.5 m/yr (Figure 4-43). The computed gradient in sediment transport potential illustrated small variations along the shoreline landward of Borrow Sites C1 north and C1 south (Figure 4-43), consistent with low shoreline change rates in Area C.

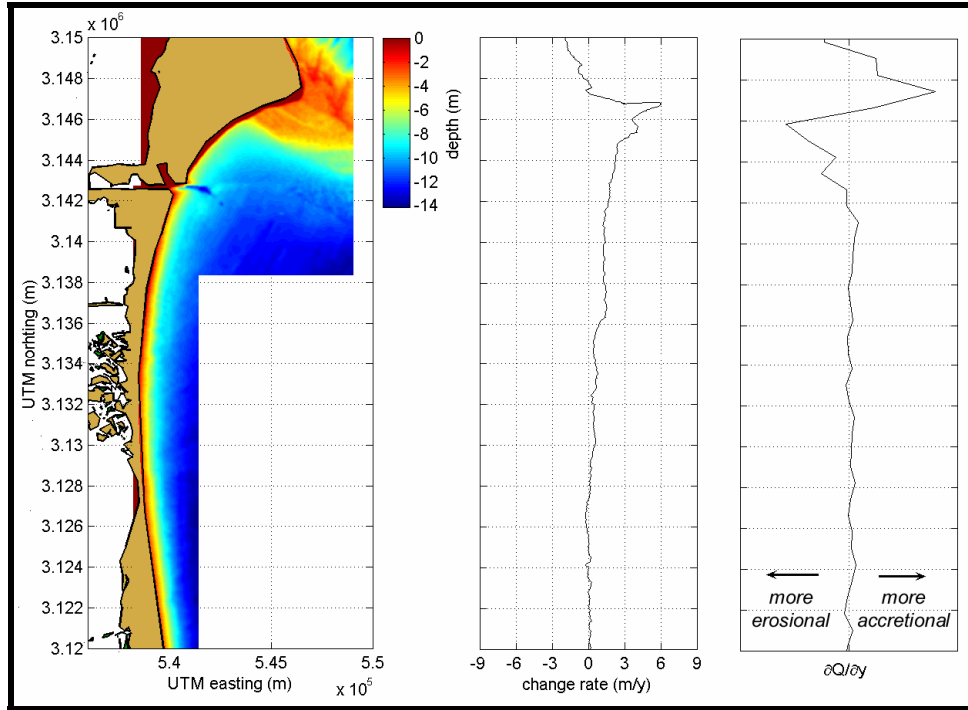


Figure 4-41. Historical shoreline change and gradient of modeled transport potential (dQ/dy) for the shoreline landward and south of Area A1. The gradient in transport potential was determined using the total net transport computed using 20 years of WIS data.

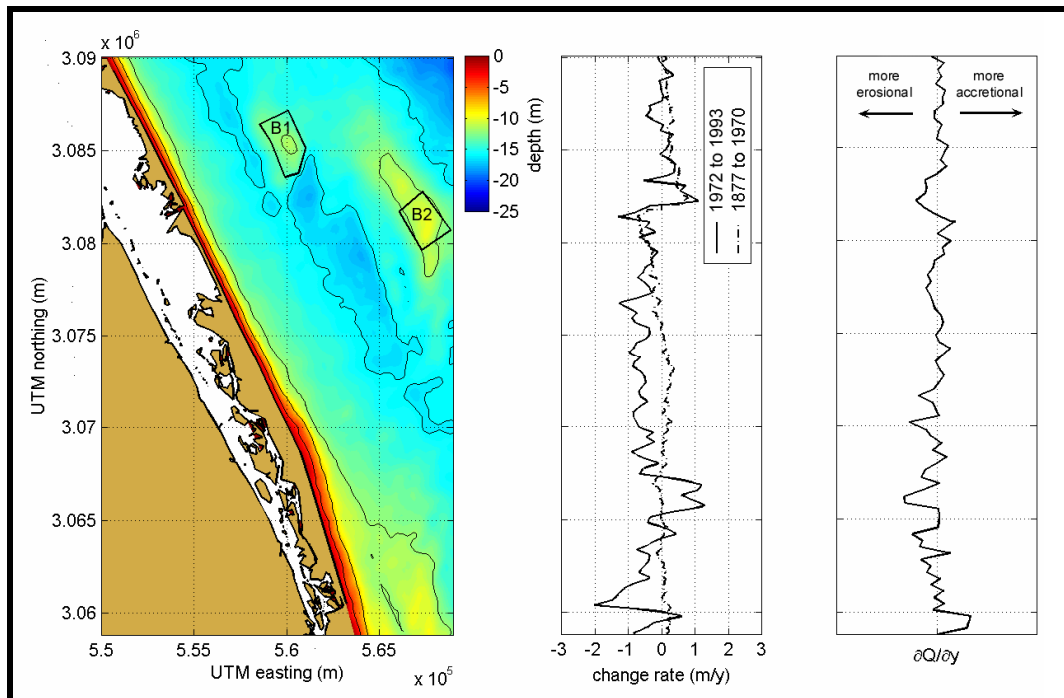


Figure 4-42. Historical shoreline change and gradient in modeled transport potential (dQ/dy) for the shoreline of Area B. The middle plot shows shoreline change for two time periods: 1877 to 1970 (black dash-dot line) and 1972 to 1993 (black solid line). The gradient in transport potential was determined using the total net transport computed using 20 years of WIS data.

For Area D (Jupiter Inlet), long-term (1887 to 1970) shoreline change rates indicated that the shoreline was stable, with change rates less than 0.5 m/yr (Figure 4-44). Short-term rates for this area illustrated much greater variation, primarily due to extensive beach nourishment projects that have been placed along this shoreline, including a 2.7 mcm project begun in 1973 for the shoreline north of the “S” curve. Because beach nourishment was included in the shoreline data, a comparison with the modeled gradient in sediment transport is less certain than with previous examples. The gradient in transport potential illustrated an area of high erosion potential located near N 2,987,200. The point of maximum negative gradient corresponds to the location of the “S” curve along the shoreline. This hot spot is not observed in either estimate of shoreline change for this area.

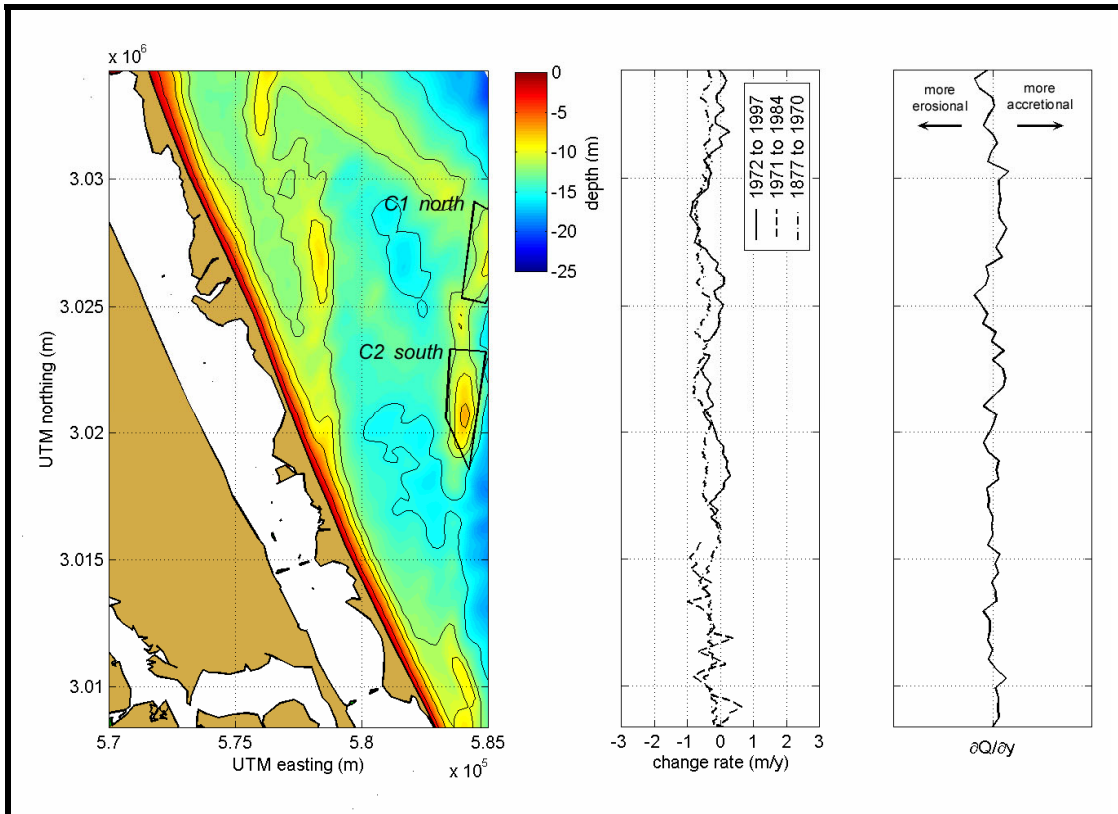


Figure 4-43. Historical shoreline change and gradient in modeled transport potential (dQ/dy) for the shoreline of Area C. The middle plot shows shoreline change for two time periods: 1877 to 1970 (black dash-dot line), 1972 to 1997 for St. Lucie County (black solid line), and 1971 to 1984 for Martin County (black dash line). The gradient in transport potential was determined using the total net transport computed using 20 years of WIS data.

4.2.2.2 Significance of Proposed Dredging

The significance of changes to longshore transport along the modeled shoreline resulting from dredging proposed borrow sites to their maximum design depths was determined using the method described in Kelley et al. (2004). For each modeled area, dredging impact significance was determined using several wave model runs in addition to the runs executed to determine the magnitude of borrow site impacts from existing to post-dredging conditions. Twenty 1-year periods were run for each area using the same directional binning as existing and post-dredging runs. Sediment transport potential was computed for each 1-year period. The standard deviation of transport potential then was

computed at each grid node, providing an estimate of annual variability in sediment transport potential along the shoreline. As such, this method incorporated the temporal and spatial variability of transport potential along the modeled shoreline. The criterion for determining dredging significance was one-half of a standard deviation ($\pm 0.5\sigma$). For modeled borrow site impacts that exceeded this limit, the borrow site would be rejected as designed.

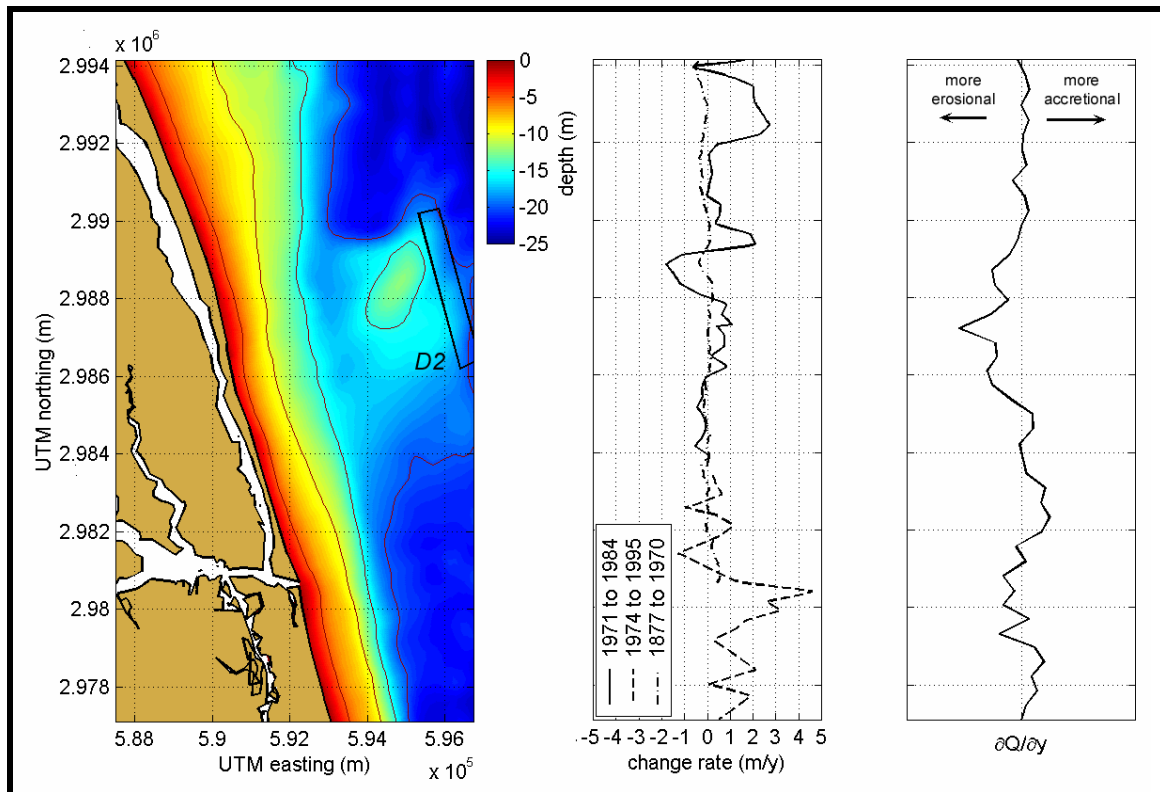


Figure 4-44. Historical shoreline change and gradient in modeled transport potential (dQ/dy) for the shoreline of Area D (near Jupiter Inlet). The middle plot shows shoreline change for two time periods: 1877 to 1970 (black dash-dot line), 1972 to 1997 for Martin County (black solid line), and 1971 to 1984 for Palm Beach County (black dashed line). The gradient in transport potential was determined using the total net transport computed using 20 years of WIS data.

Model output for the region south of Cape Canaveral indicated that the significance envelope was approximately 20% of the mean computed net transport potential in the area of greatest impact from the borrow site in Area A1 (Figure 4-45). The maximum modeled decrease in south-directed transport for post-dredging conditions was about a 40,000 m^3/yr , just south of Port Canaveral. The modeled sand excavation volume of 13.6 mcm was considerably greater than the estimated 3.4 mcm for present beach nourishment requirements in Brevard County (USACE, 1999a). Although the modeled difference was within the transport significance envelope, the magnitude of impact resulting from cumulative dredging extraction at this site may require further analysis to ensure that no detrimental impacts occur.

Due to the influence of Cape Canaveral and the series of migrating ridges and troughs on Canaveral Shoals, a direct relationship between observed shoreline change and the modeled longshore gradient in sediment transport potential could not be established. Therefore, the utility of comparing changes in sediment transport potential associated with sand mining to natural variability in longshore sediment transport may have limited applicability in this region.

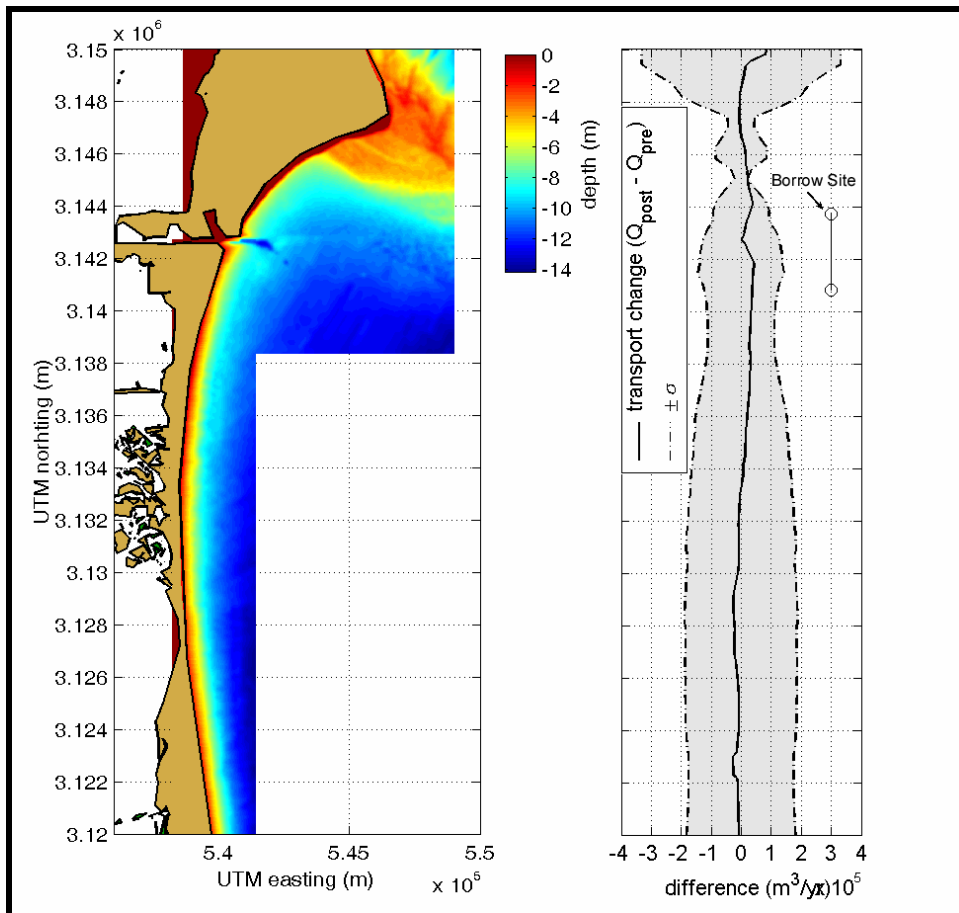


Figure 4-45. Transport potential difference between existing and post-dredging conditions, with transport significance envelope for the shoreline landward and south of the borrow site in Area A1. Negative change indicates that the post-dredging transport potential is more southerly than the computed existing transport potential.

This is most clearly illustrated by the change in transport rates at the northern limit of the model grid, where a decrease in south-directed transport of 80,000 m³/yr is predicted. Because STWAVE does not explicitly include the influence of wave diffraction, modeled transport rates in regions influenced by diffraction may not be reasonable. For cases where wave diffraction is a dominant component of wave propagation through a borrow site and to the shoreline, a spectral wave model that explicitly incorporates the influence of wave diffraction may be more beneficial for predicting potential impacts of borrow site excavation. For Brevard County, the region influenced by wave diffraction was north of Port Canaveral.

For the Area B borrow sites, the $\pm 0.5\sigma$ significance envelope was at a nearly consistent level of $\pm 100,000$ m³/yr (Figure 4-46). The impacts that result from dredging

Borrow Sites B1 and B2 occur within this envelope, indicating that these sites would not produce significant modifications to coastal processes along the shoreline. Dredging impacts were computed by subtracting the transport potential curve computed for existing conditions from the transport potential computed for post-dredging conditions. The largest calculated differences between existing and post-dredging transport potential occurred north of Sebastian Inlet (where the transport rate becomes more southerly by 30,000 m³/yr) and just south of the inlet (where transport rates become less southerly by 30,000 m³/yr).

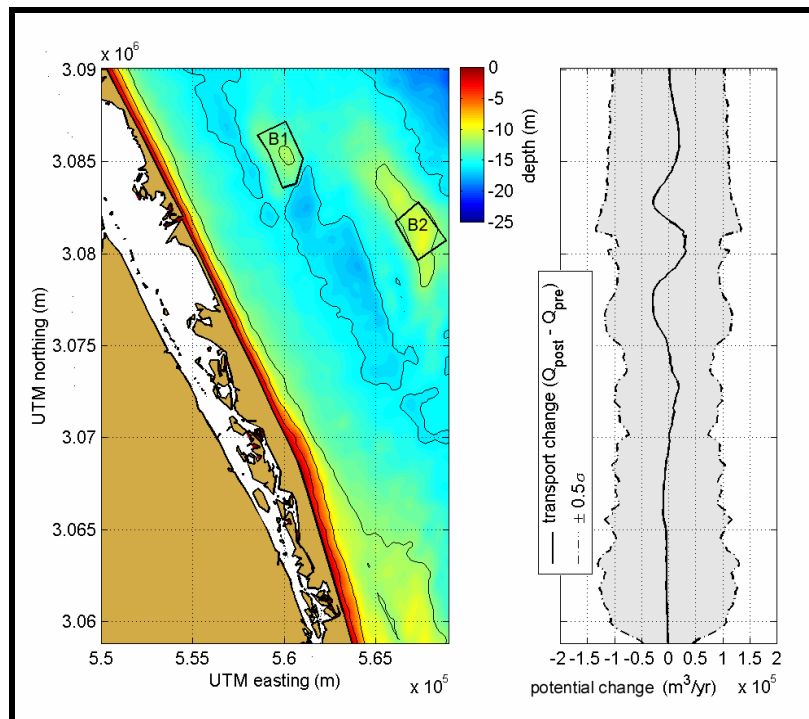


Figure 4-46. Transport potential difference between existing and post-dredging conditions, including the natural transport variability envelope for Area B borrow sites. Negative (positive) change indicates that the post-dredging transport potential is more southerly (northerly) than the computed existing conditions transport potential.

For Borrow Sites C1 north and C1 south, the $\pm 0.5\sigma$ significance envelope computed for this area ranged from approximately $\pm 100,000$ m³/yr at the northern limit of the area to $\pm 50,000$ m³/yr at the southern limit (Figure 4-47). The potential impacts from dredging Sites C1 north and C1 south to the depths shown in Table 4-6 indicated that the significance envelope was exceeded along a 2-km length of shoreline approximately 18 km north of St. Lucie Inlet. At the point of maximum dredging-induced change along the shoreline, the significance level was $\pm 60,000$ m³/yr, and the computed change in transport potential was 85,000 m³/yr. As designed, this borrow site configuration may not be acceptable. If a borrow site redesign were required, the most likely change would be a reduction in maximum dredging depth to reduce site impacts.

The envelope of significant change in transport rates under natural wave propagation conditions for Borrow Site D2 in Area D ranged from approximately $\pm 50,000$ m³/yr in the north to $\pm 100,000$ m³/yr in the south, with a maximum of approximately $\pm 150,000$ m³/yr occurring south of the "S" curve (Figure 4-48). Modeled dredging impacts to transport potential for Site D2 were minimal; predicted changes were well within the transport

variability significance envelope. Maximum dredging impacts to transport potential were approximately $\pm 10,000 \text{ m}^3/\text{yr}$. The small impacts for this area (compared with previous modeled areas) resulted from larger borrow site depths, smaller excavation volume, and the sheltering effect of the shoal landward of D2.

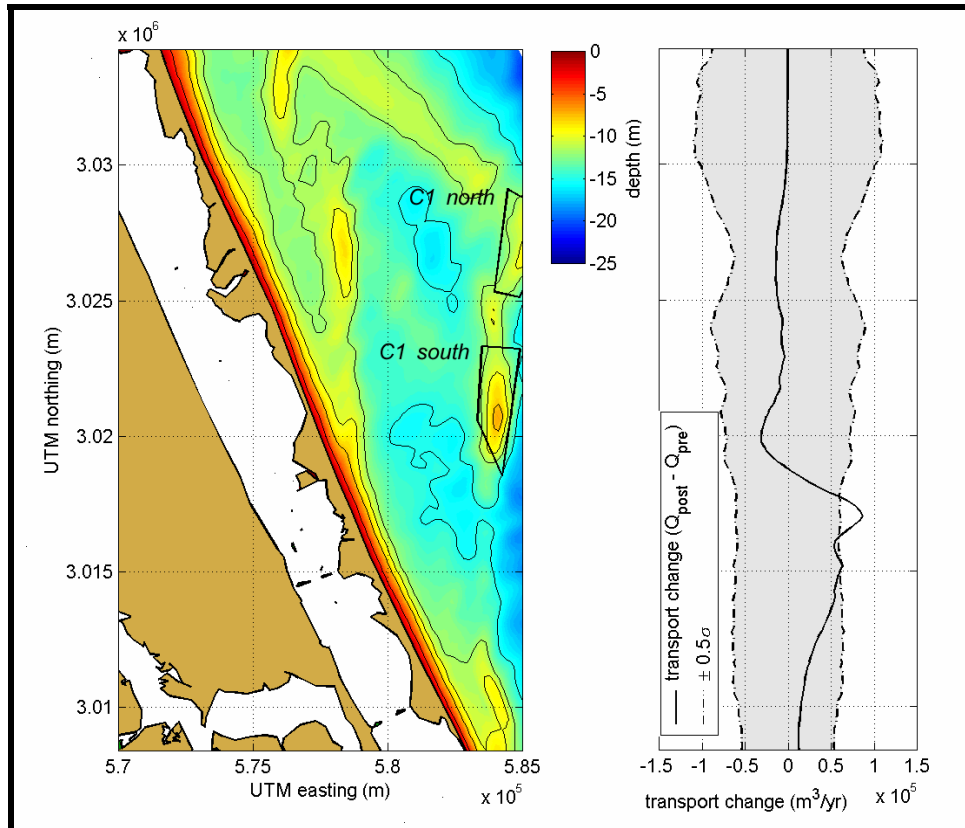


Figure 4-47. Transport potential difference between existing and post-dredging conditions, including the natural transport variability envelope for Area C borrow sites. Negative (positive) change indicates that the post-dredging transport potential is more southerly (northerly) than the computed existing conditions transport potential.

4.3 SUMMARY

This section documented results of wave modeling and sediment transport potential computations performed to assess the significance of impacts that may result from dredging sand at six proposed borrow sites offshore central east Florida. STWAVE simulated how wave fields were modified by bathymetry offshore Florida. Dominant wave conditions were developed using the 20-year WIS wave hindcast for stations offshore borrow sites in central east Florida. The same wave conditions were run for existing and post-dredging conditions. Wave model output was then used to determine sediment transport potential along the entire shoreline. Alongshore variations in the computed gradient of sand transport was compared to measured shoreline change to ensure that spectral wave modeling and associated longshore sediment transport potential could be used effectively to evaluate long-term alterations to the littoral system.

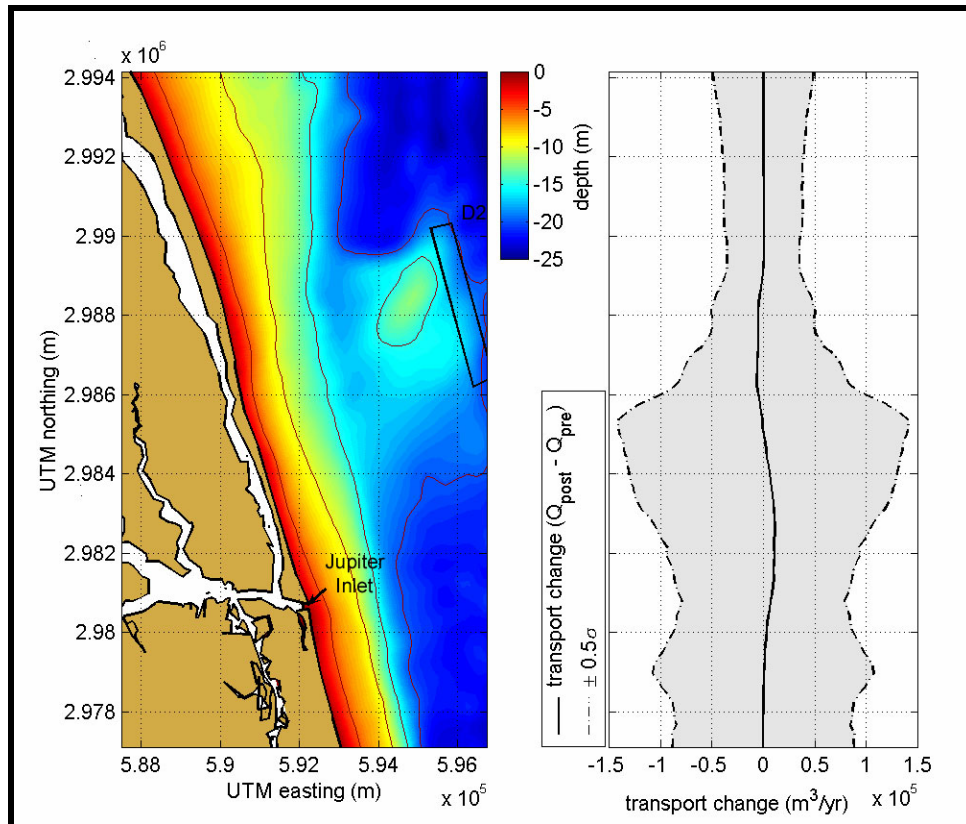


Figure 4-48. Transport potential difference between existing and post-dredging conditions, including the natural transport variability envelope for Borrow Site D2 in modeled Area D. Negative (positive) change indicates that the post-dredging transport potential is more southerly (northerly) than the computed existing conditions transport potential.

Once the change in sediment transport potential was determined for existing and post-dredging conditions, the significance of these changes was evaluated by applying a criterion developed by Kelley et al. (2004) based on the natural temporal and spatial variability of sediment transport along a modeled coastline. Each of the 20 years in the WIS record were modeled individually to determine the significance criterion envelope. The standard deviation of sediment transport potential then was computed for each modeled area. A determination of dredging significance was made by comparing predicted change in transport potential between existing and post-dredging conditions to a significance envelope of ± 0.5 to 1σ in natural transport variability along the shoreline. It was determined that no significant changes in longshore sediment transport potential would result from modeled borrow site configurations for Areas A, B, and D. However, the proposed sites in Area C do have significant impacts to transport potential along the shoreline. Therefore, Area C sites should be redesigned so impacts occur within acceptable limits, most likely by reducing the maximum depth of excavation at the sites.

